1 **The marine methane cycle in the Canadian Arctic Archipelago during summer.**

2 Alessandra D'Angelo[1], Cynthia Garcia-Eidell[2], Zak Kerringan[1], Jacob Strock[1], Frances Crable[2], Nikolas
3 VanKeersbilck[3], Humair Raziuddin[2], Theressa Ewa[2], Samira Umar[2], Andrew L. King[4], Miquel Gonzelez-
4 Meler[2] and Brice Loose[1]

5

6 [1]University of Rhode Island, Graduate School of Oceanography, Narragansett, RI 02882, USA
7 [2]University of Illinois at Chicago, Chicago, IL 60607, USA
8 [3]University of Iceland, 102 Reykjavík, Iceland
9 [4]Norwegian Institute for Water Research, 0579 Oslo, Norway

10

11 Corresponding author: Alessandra D'Angelo, a_dangelo@uri.edu

12

13 **Abstract**

14 In the Arctic Ocean region, methane concentrations are higher than the global average; high concentrations
15 of dissolved CH_4 are detectable especially across many subarctic and Arctic continental shelf margins. Yet
16 the Arctic Ocean appears to emit only minimal methane fluxes to the atmosphere across the air-sea
17 interface, suggesting water column oxidation of methane may be an important process. Here we paired
18 thermohaline, chemical, and biological data collected during the Northwest Passage Project transit through
19 the Canadian Arctic Archipelago (CAA) waters in the Summer of 2019, with in-situ and in-vitro methane
20 data. Our results showed high meltwater (meteoric water + sea ice melt) throughout the Western CAA and
21 Croker Bay in the East, and these surface meltwaters showed methane excess. The meteoric waters showed
22 a strong correlation with chlorophyll-α fluorescence (r=0.63), as well as a correlation between dissolved
23 $[CH_4]$ and chlorophyll-α fluorescence (r=0.74). Methane oxidation rate constants were highest in
24 Wellington Channel and Croker Bay surface waters (av. 0.01 ± 0 d^{-1}), characterized by meltwaters and
25 Pacific-origin waters. The average oxidation rates in meteoric and Pacific waters were respectively 24.4%
26 and 12.6% higher than the entire survey average. Moreover, Pacific and meteoric waters hosted microbial
27 taxa of Pacific-origin that are associated with methane oxidation, *Oleispira* (γ-proteobacteria), and
28 *Aurantivirga* (Flavobacteria). The deeper layers were characterized by low methane concentrations and low
29 methane oxidation rate constants (av. 0.004 ± 0.002 d^{-1}). Sea ice covered much of the Western CAA, in the
30 same region with high sea ice meltwater concentrations. These waters also hosted higher average methane
31 oxidation rates (av. 0.007 ± 0.002 d^{-1}). To the east, open coastal water coincided with methane enrichment,
32 but low chlorophyll fluorescence and weak methane oxidation. These results suggest that methane
33 production in ice-associated Arctic blooms may be quickly oxidized by microbes that are also found in
34 these waters, associated with seasonal biology.

35

36 **1. Introduction**

37 Methane (CH_4) is a climate-relevant gas with an equivalent warming potential 28 times more potent than
38 carbon dioxide over a 100-year timescale (Pachauri et al., 2014); after carbon dioxide, it is responsible for
39 about 23% of climate change in the twentieth century. The major source of methane to the atmosphere is
40 the anthropogenic emission arising primarily from agriculture, fossil fuel production, and use of waste
41 disposal; the remaining 20% of methane emissions come from minor sources such as wildfire, biomass
42 burning, permafrost, termites, dams, and the ocean (Saunois et al., 2020). In the Arctic region, methane
43 concentrations are 8–10% higher than the global average, with 1890 ppb, where ppb is used to abbreviate
44 nmol mol^{-1}, dry air mole fraction (Saunois et al., 2020; Oh et al., 2020). High concentrations of dissolved

45   CH_4 in the subarctic and Arctic shelf areas were measured in recent studies (Ferré et al., 2020), however
46   other studies showed a limited gas exchange at the air-sea interface (e.g., Fisher et al., 2011).
47   Understanding the role of the marine microbial metabolism associated with methane production and
48   oxidation is an important factor for assessing the methane venting into the atmosphere. In the water column,
49   microbial methane oxidation is an important sink for dissolved CH_4 over some depth ranges and at some
50   locations (e.g., Mau et al., 2013, Uhlig et al., 2018). In an aerobic environment, obligate aerobic bacteria
51   from the phyla *Proteobacteria* and *Verrucomicrobia* have been found to oxidize methane with oxygen as
52   an electron acceptor (Dunfield et al., 2007; Pol et al., 2007). Traditionally, the proteobacterial methane-
53   oxidizing bacteria (MOB) were divided into three groups, type I, II, and X MOB, mainly based on (i) the
54   arrangement of their intracytoplasmic membranes, (ii) their pathway for carbon assimilation and (iii) their
55   major cellular fatty acids (Hanson and Hanson, 1996). Currently, with 16S rDNA and functional gene
56   phylogeny, these divisions still hold. The type II MOB are positioned within the Alphaproteobacteria and
57   the type I and type X MOB form two distinct clades within the Gammaproteobacteria
58   (http://hdl.handle.net/1854/LU-3230105; Hoefman, 2013). Methane-derived carbon is also assimilated in
59   nonmethane-utilizing methylotrophs (non-MOB methylotrophs) or other bacteria in freshwater and
60   temperate marine environments (Saidi-Mehrabad et al., 2013).
61   Environmental drivers control the methanogenesis (microbial production of methane in hypoxic or anoxic
62   environments) and the methanotrophy (microbial aerobic oxidation of methane), by supplying suitable
63   substrates for the metabolic processes. For example, strengthened upwelling stimulates the formation of
64   phytoplankton blooms (Kudela et al., 2010), enhancing the production of dimethylsulfoniopropionate
65   (DMSP) and increasing the formation of marine particles. This could trigger CH_4 production (Damm et al.,
66   2008; Florez-Leiva et al., 2013; Dang & Lovell, 2016), despite aerobic waters, as it could be utilized as a
67   C source in the methylotrophic methanogenesis. This phenomenon may be one version of the "marine
68   methane paradox", which has received significant attention in recent years from the biogeochemical
69   community, as it drives methane supersaturation in the surface waters of most of the world's oceans with
70   respect to atmospheric concentrations (Karl et al., 2008; Sasakawa et al., 2008; Damm et al., 2015; Repeta
71   et al., 2016; Lenhart et al., 2016). The "marine methane paradox" has been explained with three main
72   processes shown in recent studies: (i) marine bacteria metabolize polysaccharide-Methylphosphonate
73   (MPn) esters through the phosphorous redox pathways in phosphate-starved environments, producing CH_4
74   as a byproduct of P acquisition (Karl et al., 2008; Repeta et al., 2016; Sosa et al., 2020); (ii) temporary
75   anoxic microenvironments could develop associated with marine particles, such as marine snow, biofilms,
76   zooplankton guts, etc. (Dang & Lovell, 2016; Poehlein et al., 2017); (iii) the phytoplankton metabolite
77   DMSP could be utilized as a C source in the methylotrophic methanogenesis, where bacteria aerobically
78   produce methane as a by-product of methylphosphonate decomposition, enhanced by the activity of
79   nitrogen-fixing microorganisms. The process is carried out by bacteria that slowly breakdown the
80   polysaccharides belonging to phytoplankton, breaking pairs of carbon and phosphorus atoms (called C-P
81   bonds) from their molecular structure. The microbes create methane, ethylene, and propylene gasses as
82   byproducts (Karl et al., 2009; Damm et al. 2009; Florez-Leiva et al. 2013). These recent research findings
83   emphasize the importance of biota in methane production and consumption; in fact, marine microbial
84   communities drive many of the biogeochemical processes in the world's oceans, including the Arctic
85   Ocean. Observations of microbial community structure can be used to identify ecosystem states, estimate
86   biological activity rates, and better understand the mechanisms underlying changes in biogeochemical
87   processes. Previous studies (e.g., Kitidis et al., 2010; Damm et al., 2010, Sultan et al., 2020; Manning et
88   al., 2020, 2022) investigated the methane flux in different regions of the Arctic Ocean, inasmuch climate-

89   relevant gases. In the Northwest Passage (NWP), a study on the methane budget revealed methane under-
90   saturation attributed to meltwater, and methane over-saturation underneath multi-year sea ice (Kitidis et al.,
91   2010), which is also supported by the multi-year observations, suggesting that riverine freshwater is not a
92   major source of CH_4 in the CAA, at least during summer and early fall (Manning et al., 2022). Moreover,
93   they assessed that the calculated rate of exchange of CH_4 between the ocean and the atmosphere was low,
94   suggesting that this region currently plays a minor role in regulating the global atmospheric concentrations
95   of methane across the North American Arctic Ocean (Manning et al., 2020, 2022). Hence, the major CH_4
96   sources in the CAA remain poorly identified.
97   In this study, we seek to further elucidate the methane budget in the NWP, quantify seawater methane
98   oxidation as a sink, and detect its main association with the environmental features and the biogenic control
99   within the water column and the sea ice. These analyses are supported by thermohaline, chemical, and
100 biological characteristics of the water masses in relation to the methane cycle. The uniqueness of this study
101 is the provision of paired datasets of the methane budget with associated marine microbial community,
102 macronutrient data, and physical properties of the water masses in the CAA. In the next section, we will
103 describe the oceanography of the Canadian Arctic Archipelago, in order to understand its hydrographic
104 regime. In section 2, we will describe the methods developed for processing and analyzing the samples. In
105 section 3, we will show the results achieved, and we will exhibit the dissolved methane data coupled with
106 the in-vitro experiments for the oxidation potential. We will observe this data encompassed with the
107 microbial taxonomy occurring in the samples, and finally, in section 4, we will discuss the outcome
108 highlighting the major sources and sinks of methane gas, and the potential hot spots of methane oxidations
109 within the study area. The result will provide the methane biogeography within the CAA.
110

1.2 Study area
112 The study area was centered around Parry Channel, between 71 – 77 °N, and 100 – 79 °W (Fig. 1). From
113 East to West, named parts of the Channel are, Lancaster Sound, Barrow Strait, and Viscount Melville
114 Sound. This Channel connects Baffin Bay with the Beaufort Sea on their eastern and western sides,
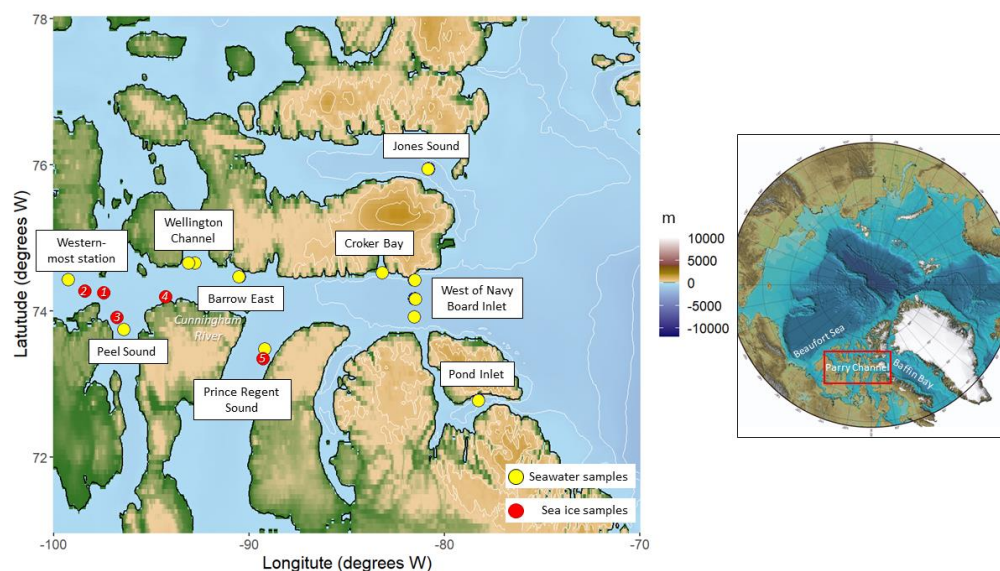115 respectively.
116

117
118 Figure 1: On the left, study area with sampling stations during the Northwest Passage cruise, July – August
119 2019. The yellow dots represent the water column sampling locations, whereas the red ones represent the
120 sea ice coring sites. On the right, international bathymetric chart of the Arctic Ocean (IBCAO, Jakobsson
121 et al., 2008), with the study area highlighted by the red rectangle.

122
123 The Arctic Ocean (AO) is characterized by a large estuarine system wherein the inputs and disposition of
124 freshwater components provide thermohaline (buoyancy) forcing (Stigebrandt, 1984; Carmack et al., 2016).
125 The CAA acts as a watershed discharge in the AO, as it is characterized by advection from the relatively
126 fresh upper layers of the AO, ice melt, local river discharge, and net precipitation (Ingram and Larouche,
127 1987). The Northwest Passage is one of three main routes connecting the AO to the Labrador Sea and the
128 North Atlantic (McLaughlin et al., 2007). There is a limiting sill within the Lancaster Sound located further
129 east in Barrow Strait, where the depth is ~125 m. Continuing eastward water depths again increase gradually
130 to ~ 500m in Lancaster Sound, then increase rapidly to over 2000 m in the center of Baffin Bay (McLaughlin
131 et al., 2007). Flow through the CAA, from the Pacific to the Arctic to the Atlantic Oceans, is due to the
132 higher sea level of the Pacific Ocean (McLaughlin et al., 2007). This sea level difference occurs because
133 Pacific waters (PW) are fresher and, assuming a level of no-motion among the three ocean basins, the Arctic
134 is thought to be 0.15 m higher than the Atlantic (Stigebrandt, 1984). During the eastward transit through
135 Parry Channel, the PW, and Atlantic Water (AW) undergoes mixing. The shallow sill at Barrow Strait
136 restricts the flow eastward across Lancaster Sound, constraining the deep layer of AW (McLaughlin et al.,
137 2007). Here, the riverine runoff supplied by Cunningham River, Garnier River, and Mecham River has a
138 big effect on the hydrodynamics and biogeochemistry of Lancaster Sound (Brown et al., 2020). The Special
139 Report on the Ocean and Cryosphere in a Changing Climate published by the IPCC in 2021, showed how
140 the runoff into the AO increased for Eurasian and North American rivers by 3.3 ± 1.6% and 2.0 ± 1.8%
141 respectively (1976–2017). Another force affecting the hydrodynamics within Parry Channel is tidal energy.
142 It enters the CAA primarily from the Atlantic Ocean and is mainly semi-diurnal. As a result, waters transiting
143 the NWP are significantly modified by tidally-driven mixing and, in the vicinity of Barrow Strait, tidal

144 currents are especially strong, reaching 50–150 cm s^{-1} (Prinsenberg and Bennetr, 1989). The water column
145 structure is characterized by AW in the deep layers, with Pacific-origin waters overlaid, and seasonal mixed
146 water at the top (McLaughlin et al., 2007). In the summer, the seasonal mixed layer contains fresh water
147 from river outflow and sea-ice melt and is characterized by low salinities (24<S<31), warm temperatures,
148 low nutrient concentrations, and high dissolved oxygen saturations. This water is the upper-most layer and
149 its depth changes accordingly to the meltwater supply (~ 50 m in depth in Parry Channel). Below this layer
150 is the Pacific-origin summer water. This water is characterized by relatively warm temperatures and higher
151 salinities (31<S<32), with higher nutrient concentrations and decreasing oxygen saturations. Atlantic-origin
152 water, within deep layers, shows maximum nutrient concentrations (McLaughlin et al., 2007). The western
153 part of the CAA is characterized by a more consistent sea-ice coverage (Agnew and Howell, 2003). The
154 information released by the Canadian Ice Service shows that the ranges of sea ice thickness of first-year ice
155 in the CAA can vary from maximum values of 2.5 m in the northern and 2.0 m in the southern sections.
156 Multi-year ice can reach a thickness of 3–5 m (Canadian Ice Service, 2002). Between freeze-up in January
157 and break-up in late July the ice is generally immobilized as landfast ice and due to strong winds, it is also
158 characterized by the occurrence of polynyas (Dunbar, 1969).
159
2. Materials and methods

161 The list of the sampling locations and acronyms used in this paper is the following (Fig. 1): Western-most
162 station (WS), Wellington Channel (WC), Peel Sound (PS), Prince Regent Sound (PRS), West of Navy
163 Board Inlet (WNBI), Crocker Bay (CB), Jones Sound (JS), Pond Inlet (PI).
164
2.1 Sampling procedures
166 Seawater and sea ice samples were collected in the vicinity of Parry Channel during the Northwest Passage
167 Project cruise held between 17 July – 4 August 2019 onboard the Swedish icebreaker RVIB Oden. The
168 stations include both single points and transects (see Fig. 1), covering the area with longitude 78°14.94' W
169 - 99°16.63' W. Seawater were collected using a SeaBird 32 Water Carousel CTD rosette (24 x 12L), set
170 with a SeaBird SBE 911+ CTD with dissolved oxygen and WETLabs Ecopuck sensors. The CTD sensor
171 was owned and calibrated by the Swedish Polar Research Secretariat (SPRS). CTD casts and rosette bottle
172 data are hosted at Swedish National Data Service (https://snd.gu.se/en/catalogue/study/2021-119#dataset),
173 whereas the whole dataset and the processed CTD data are stored in Arcticdata.io
174 (https://doi.org/10.18739/A2BN9X45M). Sea ice cores were sampled with a Kovacs ice corer drill. The sea
175 ice concentration data was provided by the University of Bremen data archive, with 10m space resolution
176 (seaice.uni-bremen.de, Spreen et al., 2008). Sea ice charts were collected by the Canada ice center
177 (www.canada.ca/en/environment-climate-change/services/ice-forecasts-
178 observations/publications/interpreting-charts).
179 *Nutrients* – A total of 239 seawater samples were collected for nutrients measurements (for
180 processed data see: https://doi.org/10.18739/A2BN9X45M). A volume of ~ 45ml sample was filtered
181 through 0.22-micron Millex-GP Sterile Syringe Filters with PES Membrane (Thermo Fischer Scientific)
182 into a Corning Falcon 50 mL Conical Centrifuge Tubes (Fisher Scientific). The samples were stored
183 onboard RVIB Oden at -20°C for post-expedition analysis.
184 *Methane* – A total of 132 (56 experimental and 76 discrete) seawater samples (Table S1) and 5 sea
185 ice cores (Table S2) were collected and analyzed for methane concentration and isotope ratio as well as the
186 microbial oxidation rate. The samples were both collected through multi-layer foil gas sampling bags
187 (Restek, Bellfonte) and processed for further analysis (see details in paragraph 2.3).

188   *Microbial community* – A total of 18 seawater samples were collected from the in-vitro methane
189 incubations at the end of the experiments, for identifying the most abundant taxa. A cylindrical, 0.22 µm
190 Sterivex membrane filter (Millipore Sigma, Billerica, MA) was connected to the valve of each bag for the
191 samples collection. We removed and sealed the filters and stored them in -80 °C freezers until they were
192 transported to the University of Rhode Island (URI), Graduate School of Oceanography (GSO) for post-
193 expedition DNA extraction, using the DNeasy PowerWater Sterivex Kit (Qiagen, Germantown, MD)
194 following the manufacturer's protocol (see details in paragraph 2.4).

195

196 **2.2 Nutrients**

197 Silicate, phosphate, nitrate, and nitrite concentrations were determined using a Quik Chem Series 8500
198 Lachat analyzer (Serial Number 061100000379 – Hach, Loveland, Colorado, USA). Heater Configuration
199 500 W Max, reagents and standards prepared using Quik Chem Protocols: Nitrate + Nitrite 31-107-04-1 A,
200 Silicate 31-114-27-1 A, Phosphate 31-115-01-1 H. The analysis was carried out at the Marine Science
201 Research Facility, URI - GSO (https://web.uri.edu/marinefacility/). To quality check the nutrients data,
202 after excluding the data showing SD>5% between the replicated measurements, we compared nutrient data
203 with datasets from literature (e.g., Torres-Valdés et al., 2013; Bhatia et al., 2021) and databases (e.g.,
204 DiTullio and Lee, 2019). When all the three measured nutrients (phosphate, nitrate+nitrite, silicate) showed
205 nonagreement with the reference data, a flag = 0 was assigned to the values, highlighting outliers (D'Angelo
206 et al., 2022 *preprint*). In total, 5 outliers were highlighted in our data frame. We also tried to identify the
207 outliers through other procedures, but these did not show high efficacy for our dataset. In this case,
208 calculating N:P:Si ratios for near Redfield-like consistency is likely not appropriate for our data, since
209 denitrification plays a big part in shaping the nutrient ratios in Pacific waters, and significant freshwater
210 inputs influence nutrients in a non-Redfield manner (Macias et al., 2019).

211

212 **2.3 Methane concentration and isotope ratio measurements for discrete and experimental samples**

213   *Samples processing* – Seawater for gas and isotope analysis was collected through vacuum multi-
214 layer foil gas sampling bags equipped with a polypropylene combo valve and septum (capacity 1L and 3L,
215 # 22950 and # 22951, Restek, Bellfonte, Pennsylvania, U.S.A.). Discrete samples were put in 3L size bags,
216 while the experimental samples were collected in 1L size bags. Experiments were performed with
217 approximately 0.8/0.9 L seawater, while discrete samples volumes were ~ 2.8 L. The sea ice cores were put
218 in 3L bags and melted at room temperature for the analysis. For each sample, a headspace with
219 hydrocarbon-free air (Airgas, Rhode Island) was made to permit multiple measurements from the same
220 sample in a time series. For incubation samples we injected a known volume (1 to 2.5 ml, see Table 1) of
221 gas standards with known concentration and isotopic composition (std. 1003: 2500ppmv, $\delta^{13}CH_4$= -66.5
222 ‰ Isometrics, Victoria, British Columbia, Canada). For the calibration of the instrument, we used additional
223 methane standards.

224

225 Table 1: Information on incubation experiments. In the table are shown only the data without discrepancy
226 between the methane oxidation rate constants of mass balance and isotope ratio.

227

Sample	CTD	Transect	Date	Depth (m)	CH$_4$ spike (ml)
22	3	Jones Sound (JS)	7/19/2019	609	1
26	3	Jones Sound (JS)	7/19/2019	7	1
36	8	West of Navy Board Inlet (WNBI)	7/23/2019	70	2.5

37	8	West of Navy Board Inlet (WNBI)	7/23/2019	15	2.5
39	8	West of Navy Board Inlet (WNBI)	7/23/2019	15	2.5
40	8	West of Navy Board Inlet (WNBI)	7/23/2019	450	2.5
41	8	West of Navy Board Inlet (WNBI)	7/23/2019	70	2.5
43	12	West of Navy Board Inlet (WNBI)	7/24/2019	743	2.5
45	12	West of Navy Board Inlet (WNBI)	7/24/2019	401	2.5
58	21	Wellington Channel (WC)	7/26/2019	10	2.5
59	21	Wellington Channel (WC)	7/26/2019	10	2.5
76	41	Prince Regent Sound (PRS)	7/31/2019	25	2.5
78	41	Prince Regent Sound (PRS)	7/31/2019	25	2.5
79	52	Croker Bay (CB)	8/3/2019	7	2.5
81	52	Croker Bay (CB)	8/3/2019	241	2.5
82	52	Croker Bay (CB)	8/3/2019	241	2.5
83	52	Croker Bay (CB)	8/3/2019	7	2.5

228

229 The bags for in-situ measurements were stored in water at room temperature (~10°C), while the
230 experimental bags were stored in a cold room onboard Oden at ~0ºC. Bags were analyzed for [CH_4] and
231 isotopic signature ($\delta^{13}CH_4$) directly after preparation, following the method of Uhlig et al. (2017).

232 *Analytic procedure* – Analysis for [CH_4] and $\delta^{13}CH_4$ was performed with a Picarro G2201-i cavity
233 ring-down spectrometer (Picarro, Santa Clara, California, U.S.A.) coupled to Small Sample Introduction
234 Module (SSIM) (Picarro, Santa Clara, California, U.S.A.) (Uhlig and Loose, 2017). The SSIM is a sample
235 inlet system useful for the determination of isotope ratios from discrete samples with a flow rate of
236 approximately 22 mL min^{-1}. The SSIM further offers the possibility to dilute highly concentrated samples
237 with hydrocarbon free zero air to reach the specification range of the analyzer of 1.8–500 ppm CH_4 (Uhlig
238 and Loose, 2017). The dilution factor was calculated from the volume of sample (V_{sample}), volume of the
239 dilution chamber (V_{SSIM}=22 mL), the pressure of the dilution gas (P_{SSIM}), and the atmospheric pressure
240 (P_{atm}) recorded onboard:

241
$$dil\ factor\ SSIM = \frac{Pssim}{\frac{Vsample}{Vssim} * Patm}$$

242 To avoid water vapor, samples introduced into the SSIM passed first through a Nafion V R tube in a
243 Permapure Gas Dryer cartridge filled with desiccant (#DM-060-24-COMP2, Permapure LLC, New Jersey,
244 U.S.A.). Sample and standard volumes injected into the SSIM using SGE gastight syringes equipped with
245 shutoff valves (1 mL, 5 mL and 10mL total volume - SGE, Victoria, Australia) varied between 0.01 mL
246 and 10 mL, respectively. The SSIM coordinator software was run on fast measurement mode, syringe
247 injection setting, and dilution with hydrocarbon-free air (Uhlig et al., 2017). The saturation capacity of the
248 in-situ samples was calculated with the Gas-Solubility Codes in R (https://github.com/URIGSO/Gas-
249 Solubility-Codes) and using in-situ potential temperature and practical salinity. For the sea ice, we used a
250 salinity of 2 from the sea ice cores averaged data.

251 *Calibration* - To obtain more reproducible data, the manufacturer recommends the use of the
252 G2201-i for methane mixing ratios >1.8 ppm (see Uhlig et al., 2017, Fig.1a). Standard gases 1001
253 (2500ppmv, $\delta^{13}CH_4$= -23.9 ‰), 1002 (250ppmv, $\delta^{13}CH_4$= -38.3 ‰), 1003 (2500ppmv, $\delta^{13}CH_4$= -66.5 ‰)
254 were used to generate linear calibrations for mixing ratios and isotope ratios in order to correct for any

255 transient deviations in the G2201-i analyzer, while the standard 1003 was used almost simultaneously
256 during the measurements to calibrate the measurements via daily drift.

257 *Estimating the oxidation rates from mass balance and isotopic fractionation* – Microbial methane
258 oxidation was determined from the methane mass balance in incubation experiments following the method
259 of Uhlig and Loose (2017). Briefly, an aliquot of methane standard with known concentration and isotope
260 ratio (pCH$_4$ = 2500 ppmv, and δ ^{13}CH$_4$ = -66.5 ‰) was added to every incubation to monitor the change in
261 moles and the isotope ratio. The time of the incubations varied between 7 and 25 days, and the samples
262 were stored in a cold bath between 0 and 1ºC.

263 For each methane incubation, we develop two independent measurements of the oxidation rate using the
264 (1) molar mass balance and (2) isotopic fractionation during oxidation/production (Uhlig and Loose, 2017).
265 During the methane microbial oxidation, the [CH$_4$] decreases overtime, due to the consumption made by
266 microbes, while the isotopic signature increase as a sign of preference towards δ^{12}CH$_4$ of microbes. The
267 reservoir of methane (M$_{tot}$) here represented the sum of the mass of methane dissolved in the water (M$_{gw}$)
268 and the mass of methane in the headspace (M$_{ghs}$) in moles.

269 $$M_{tot} = M_{gw} + M_{ghs}$$

270 As the measurements were repeated on the same sample at each time, it was important to account for the
271 decrease in the headspace volume which affects the numbers of moles of methane that can transfer to the
272 water for oxidation. Before calculating the oxidation rate, the total mass of CH$_4$ was corrected for the mass
273 removed during sampling to obtain as in appendix A, Uhlig et al. (2017). It is routine to assume that
274 microbial methane oxidation can be modeled as a first order kinetic process during the exponential oxidation
275 phase (Reeburgh et al., 1991; Valentine, 2002).

276 $$\ln\left(\frac{Mtot_{corrected_{ti}}}{Mtot_{corrected_{t-1}}}\right) = k_{ox} * t_{i-i-1}$$

277 Where $Mtot_{corrected_{ti}}$ was calculated as:

278 $$Mtot_{corrected_{ti}} = Mtot_{ti} + \sum_{i=0}^{j=t_i-1} M_{sampled}$$

279 Therefore, the oxidation rate constant k$_{ox}$ (with units of time^{-1}) was determined as the negative slope of the
280 linear regression of ln($Mtot_{corrected}$) and the incubation time (ti). Conventionally, a positive k$_{ox}$ indicates
281 a decrease in methane concentration, while a negative kox indicates an increase. Molar quantities of
282 methane in the headspace (M$_{g\_hs}$) and water (M$_{g\_w}$) were calculated as equilibrium concentrations according
283 to Magen et al. (2014) with the equilibrium constant according to Yamamoto et al. (1976). In addition to
284 the decrease in the total mass of CH$_4$ caused by microbial oxidation of CH$_4$, the carbon isotope ratio of the
285 remaining methane pool changes due to isotopic fractionation (Whiticar, 1999). The fractionation factor
286 α_{ox}=k$_{12}$/k$_{13}$ (Mahieu et al., 2006) is the ratio of the kinetic constants for reactions of the heavier (k$_{13}$) and

287 lighter (k$_{12}$) isotope CH$_4$ (Uhlig et al., 2017 - Appendix B). By plotting ln$\frac{\left(\frac{1000+\delta13CH4_{ti}}{1000+\delta 13CH4_{t0}}\right)}{\left(\frac{1}{\alpha ox}-1\right)}$ vs. t, the first

288 order oxidation rate constant derived from δ ^{13}CH$_4$ (k$_{ox.delta}$) was determined as the negative slope of the
289 linear regression. A positive k$_{ox.delta}$ indicates an increase in δ ^{13}CH$_4$, and a negative k$_{ox.delta}$ a decrease. Cold
290 marine environments with temperatures below 28ºC record fractionation factors in the range of 1.002–1.017
291 (Cowen et al., 2002; Grant & Whiticar, 2002; Damm et al. 2007; Fenwick et al., 2017), but for *in-situ* data
292 it must be taken in account the mixing effects in the water column (Grant & Whiticar, 2002). As in Uhlig

293   eth al. (2017), this study used α_{ox} of 1.007 as lower bounds. The microbial oxidation rates were calculated

294   from the first order rate constant k_{ox} and the methane concentration dissolved in the water $[CH_4]_w$ during

295   the incubation experiments as $r_{ox}= k_{ox} * [CH_4]_w$ (Uhlig et al., 2017). To validate the reproducibility of the

296   data, we plotted the comparison of first order rate constants determined from concentration ($k_{ox,mass.balance}$)

297   and isotope ratio ($k_{ox,isotope.ratio}$) (Fig. 2). The trend line in Figure 2 showed linear correlation of 0.52 by the

298   Spearman's rank.

299

300
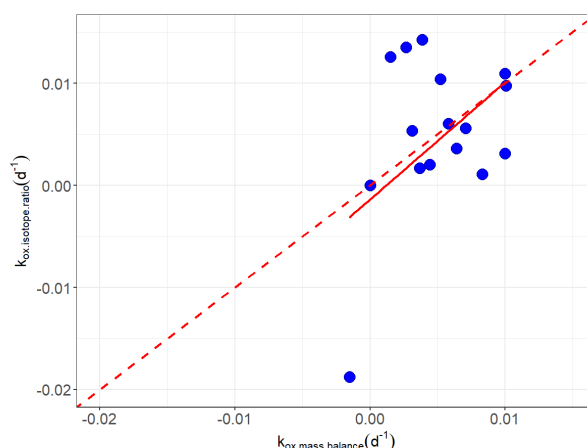
301   Figure 2: Comparison between first order oxidation rate constants (k_{ox}) determined from CH_4 concentration

302   (mass balance) and isotope ratios. The red line displayed the linear model between the values (R-squared:

303   0.2564 p-value: 7.985e-12), whereas the red dashed line represented the 1:1 regression line.

304

305   To assess the success of the experiments and measure the microbial activity, a killed control was prepared

306   for each sample by adding 0.1M NaOH and injecting it into the sample after the t_{final} measurement. For 1L

307   sample, we diluted 4 g NaOH pellets in 100ml MilliQ and injected 10ml solution into the sample. The

308    $[CH_4]$ and $\delta^{13}C-CH_4$ were measured three times within one week time frame.

309   *Quality control* - The measurements of methane concentration were not calibrated, because the

310   standard deviation between replicate dissolved methane water samples was significantly smaller than the

311   standard deviation in gas standards that were introduced to the Picarro analyzer, likely due to a manual

312   artifact during syringe sampling of the gas standards. A complete calibration of $\delta^{13}CH_4$ isotope ratio was

313   carried, because the isotope ratio was not affected in the same way as concentration during syringe sample.

314   Linear calibration equations were determined using three standards 1003: 2500ppmv, $\delta^{13}CH_4$ = -66.5‰;

315   1002: 250ppmv, $\delta^{13}CH_4$= -38.3 ‰; 1001: 2500ppmv, $\delta^{13}CH_4$= -23.9 ‰; the standard 1003 was used for

316   calculating the daily drift of the instrument. The 1003 standard revealed distinct instrumental drift while

317   onboard the vessel Oden, as compared to the measurements on land; hence, we evaluated the dataset in two

318   periods, from July 19th to August 4th (when the data were measured at sea), and from August 5th to August

319   14th (when the data were measured in the National Science Foundation facilities at Thule airbase,

320   Greenland). For the isotope ratio, we calculated the slope and intercept of the standard 1003 overtime and

321   used the slope and intercept from the days of full calibrations (July 19 and July 29) into the equation for the

322   data correction.

$$data.corrected = slope.day.cal * (data - std.1003.overtime) + (-66.5)$$

Where, -66.5 ‰ was the expected isotope ratio of the standard 1003.

Statistical criteria used to determine the oxidation rate: Duplicate in-vitro bag samples were collected for every in-vitro determination of methane concentration. This gives a matrix of 2 bags x 2 independent measurements (mass balance and isotopic fractionation) to make a robust determination of methane oxidation. The criteria that were used for this determination were as follows:

1. For each in-vitro bag, the slope in molar mass and isotope ratio, described above was subjected to a significance test using the Student's T distribution, to ensure that the slope or the rate of change in [CH_4] or $\delta^{13}CH_4$ vs. time (oxidation or production rate) was unique from zero, within error. The number of independent measurements for each incubation was less than 15 (N<15), and we chose a confidence interval of 0.95.

2. Next, we compared the isotope ratio and molar mass determination between both bags, for quality check. First, we picked the bags showing agreement between the isotope ratio and the molar mass oxidation constants ($k_{ox.mass.balance}$ and $k_{ox.isotope.ratio}$ showing same sign). The samples showing discrepancy within the $k_{ox,mass.balance}$ and $k_{ox,isotope.ratio}$ were flagged with "0" in the final dataset (N= 37 over N_{tot}=56) and they were not considered in this manuscript.

3. Once selected the sub-dataset, we removed data showing discrepancies within the null hypothesis (for example, for the same sample we had $k_{ox.mass.balance}$ accepting and $k_{ox.isotope.ratio}$ rejecting the null hypothesis). In some cases, the whole matrix 2x2 did not show the same outcome, and we selected only data showing at least 3 agreements over 4 (2 x mass balance and 1 x isotope ratio, or vice versa).

4. The full analyses were performed with the software package R version 4.1.2 in RStudio Version 1.2.5033. Plots were prepared with base and ggplot2 packages.

Using these criteria, we can determine a definitive rate of methane oxidation vs. no measurable rate of methane oxidation. We consider a rate of 'no detectable oxidation' to also be a scientifically useful outcome because it provides a census and biogeography for where and how frequently microbial oxidation is taking place. A third outcome of the incubations can be methane production. Our experiments are not well set up to measure this as we add methane of a known isotope ratio, which might overwhelm methane produced by microbes. Nevertheless, some samples revealed methane production although all did not pass the statistical criteria described above.

2.4 DNA extraction and sequencing

Methane-oxidizing communities from seawater were analyzed for their entire community diversity (16S rRNA gene sequencing) from methane incubated samples at time 'Final' of the experiment (Uhlig et al., 2018). DNA was extracted with the PowerWater® DNA extraction kit (MoBio, Carlsbad, California, USA). The DNeasy PowerWater Sterivex Kit was used to isolate genomic DNA from Sterivex filter units (Millipore® cat. no. SVGPL10RC) without the need for enzymes or hazardous organic chemicals. Inhibitor Removal Technology® (IRT) was included to provide high-quality DNA from all types of water samples, even those containing heavy amounts of contaminants. In addition, MB Spin Columns and tube extenders allowed for one-step addition of the entire sample lysate (4.5 ml) and elution in a 50–100 µl volume. The DNeasy PowerWater Sterivex Kit protocol started with the addition and incubation of the Sterivex units with a novel filter membrane treatment. Lysis buffer was added to the units, which were then mixed. The lysate was then removed for additional mechanical lysis in a 5 ml bead beating tube. After the protein and inhibitor removal steps, extracted genetic material was captured on an MB Spin Column under vacuum.

367 The column was washed, and high-quality DNA was eluted from the MB Spin Column filter membrane for
368 use in downstream applications, including PCR and qPCR.

369   *PCR amplicon construction and sequencing* - From each extract, the V4-V5 hypervariable region
370 of the 16S rRNA gene were amplified using forward and reverse primers from Parada et al., 2016. A 20-µl
371 PCR reaction was performed for each sample which contained a mixture of 0.4 µl Platinum SuperFi II DNA
372 Polymerase (Invitrogen, Carlsbad, CA), 4 µl SuperFi II Buffer (5x), 0.2 mM dNTPs, 0.5 µM of each primer,
373 and 0.1 µl Bovine Serum Albumin (Thermo Scientific, Carlsbad, CA). We amplified each water sample in
374 a single PCR reaction with 5 µl of DNA template. To account for possible PCR reagent contamination
375 during PCR amplification, three samples were amplified (one for each batch of polymerase used), each one
376 containing only laboratory water and no extract. Additionally, we completed the full DNeasy
377 PowerWater Sterivex protocol using a sterile Sterivex filter for each kit to account for possible kit
378 contamination. The thermal cycler program for all reactions began with an initial denaturation temperature
379 of 98°C for 30 seconds followed by 35 cycles of 98°C for 10 seconds, 60°C for 10 seconds, and 72°C for
380 15 seconds, followed by a final extension of 72°C for 5 minutes. We cleaned all the samples using the
381 Agencourt AMPure PCR Purification Kit (Beckman Coulter Life Sciences, Indianapolis, IN). Finally, all
382 samples were sent to the University of Rhode Island Genomics and Sequencing Center and sequenced on
383 an Illumina MiSeq platform using the Illumina MiSeq V3 chemistry at 2 x 300 cycles (NCBI BioProject
384 PRJNA718862).

385

386 **2.5 Water mass detection**
387 Water masses were defined by a linear mixing model, the multiparameter analysis (Tomczak,1981). The
388 contribution of each Source Water Masses (SWM, fi) was estimated for each measured point using an
389 ordinary least squares method. The obtained fi values are in the range 0–1 and refer to the amount of a
390 certain SWM ''i'' that is implicated in the mixing processes (Pardo et al., 2012; Newton et al., 2013). The
391 SWMs in our study were: Atlantic Water (AW), Pacific Water (PW), Meteoric Water (MW) and Sea Ice
392 Meltwater (SIM). We applied SA, δ18O, and an N:P-based tracer (ANP) to calculate the fractions of each
393 sample. The endmembers were chosen according to our dataset and previous literature: for salinity, we used
394 both extreme values (for AW and PW) and values from the literature for MW and SIM (Whitmore et al.,
395 2020; Newton et al., 2013; Ekwurz et al., 2001); for ANP we followed Newton et al., (2013); finally, for
396 $\delta^{18}O$ we used the extreme values for AW and PW, MW= -20 (Whitmore et al., 2020), and SIM= surface
397 values per CTD + 2.6 ‰ (as in Newton et al., 2013).

398 $$f_{AW}+f_{PW}+f_{MW}+f_{SIM}=1$$

399 $$f_{AW}(SA)+f_{PW}(SA)+f_{MW}(SA)+f_{SIM}(SA)=SA_{obs}$$

400 $$f_{AW}(ANP)+f_{PW}(ANP)+f_{MW}(ANP)+f_{SIM}(ANP)=ANP_{obs}$$

401 $$f_{AW}(\delta^{18}O)+f_{PW}(\delta^{18}O)+f_{MW}(\delta^{18}O)+f_{SIM}(\delta^{18}O)=\delta^{18}O_{obs}$$

402 A more detailed description of the method can be found in D'Angelo et al., 2022 *preprint*
403 (https://doi.org/10.5194/essd-2022-306).

404

405 **3. Results**

406

407 **3.1 Nutrients**

408   Phosphate, silicate and nitrate + nitrite concentrations were measured within the water column for each site.
409   In Fig. 3, the complete vertical profiles are displayed for each nutrient, along the longitudinal transect. The
410   spatial scale highlighted the Pacific-origin waters containing elevated nutrients (blueish).
411
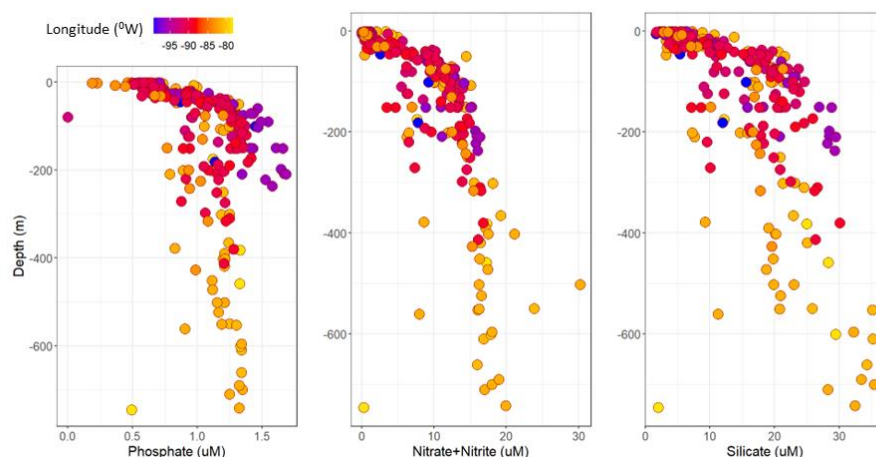
412

413   Figure 3: Phosphate, nitrate + nitrite, silicate concentrations (µM) along the CAA water column. The
414   vertical profiles are colored by longitude of the data sites, with the most negative longitudes reflecting the
415   western-most stations of the NWP expedition, furthest from Baffin Bay and the North Atlantic.
416

417   The concentrations range from 0 to 1.7 µM for phosphate, 1.7 to 35.4 µM for silicate and 0 to 30 µM for
418   nitrate + nitrite. Overall, nitrate+nitrite and silicate concentrations exhibit a monotonic increase with water
419   depthwith the exception of phosphate that had concentration maxima around 200m depth in PWs of the
420   westernmost stations (~95 ºW, purplish in the color scale of Fig. 3). Nitrate+nitrite and silicate exhibited
421   highest concentrations within deeper AW layers, especially toward the east (~80-85 ºW, yellowish in the
422   color scale of Fig. 3).
423

424   **3.2 Dissolved methane and isotope ratio profiles within the water column.**
425   The seawater equilibrium supersaturation of methane in the CAA, relative to the atmospheric methane
426   concentrations 3.42±0.05 nM, varied across space and time due to variability in temperature and salinity.
427   The surface waters (surface to ~40 m) of the CAA mostly exceeded equilibrium saturation of CH_4, up to a
428   maximum of 362%, while in the deeper layers methane saturation anomaly was <~100% (Fig. 4). According
429   to the color scale in Figure 4, the methane enrichment and depletion across a longitudinal scale did not
430   show a clear trend.
431
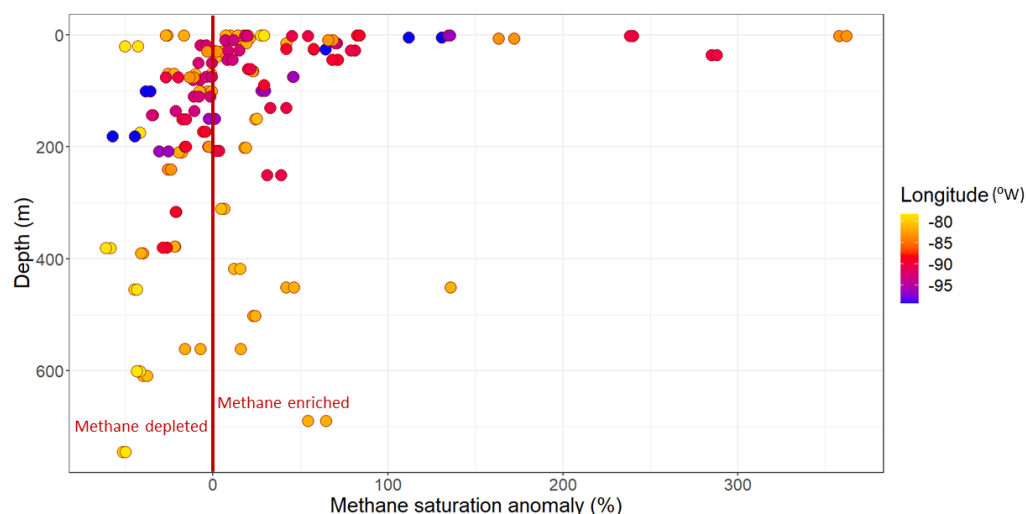
432
433 Figure 4: Methane saturation anomaly vertical profile, colored by longitude. The saturation anomaly was
434 calculated as ([CH$_4$]$_{in\text{-}situ}$ / [CH$_4$]$_{equilibrium}$ − 1) *100, considering the solubility of the atmospheric methane
435 at in-situ marine T and S. The dark red line indicated the methane concentrations at the equilibrium with
436 the atmospheric methane concentration.
437
438 The weak negative correlation between CH$_4$ and salinity (Fig. S1) suggests that freshwater is associated
439 with higher [CH$_4$], but this may be a result of both salinity and CH$_4$ negatively covarying with depth. Figures
440 5 a and b show the discrete methane profiles of isotope ratio (a) and concentration coupled with the methane
441 concentration at the atmospheric equilibrium (b) in Croker Bay. Croker Bay represented the site with the
442 highest supply of meltwater (mainly meteoric origin, MW) and recorded the highest methane concentration
443 (Fig. 5b, ~17nM) coupled to the lowest isotopic signature (Fig. 5a, ~-64.3 ‰). The very depleted isotopic
444 signature could be a result of subglacial methanogenesis (Pain et al., 2020). In Croker Bay, the subsurface
445 [CH$_4$] was close to atmospheric equilibrium, while concentrations were higher in the upper 25 m (Fig. 5b).
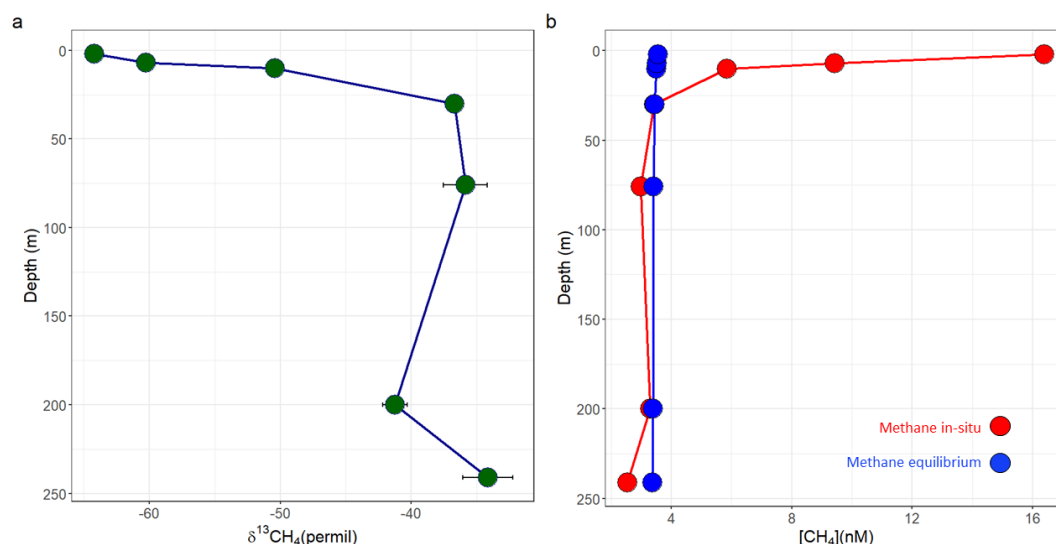446

Figure 5: Methane data from samples collected in Croker Bay. a) methane isotope ratio profile; b) dissolved methane profile along the column water (methane in-situ) and methane concentration at the equilibrium relative to the atmosphere capacity (methane equilibrium).

Overall, the range of methane concentrations values varied between 2 and 17 nM across the entire dataset, whereas the isotope ratio varied between -64.2 and -17 ‰, with lowest isotope ratios in the surface ocean. The average of the [CH$_4$] was 4.17 ± 2.5 nM, and the values below the average were recorded within deeper layers (av. depth = 190m). West of Navy Board Inlet was the only site showing deep water methane enrichment, with ~3 nM higher concentrations in deeper layers. At this site, we recorded high turbidity within deep layers, possibly suggesting methane released from sediments (Damm et al.,2005; Graves et al., 2015; Silyakova et al., 2020). Overall, the entire data set, there is an inverse correlation (R^2: 0.35, slope = -0.18) (Figure 6) between methane concentration and isotope ratio, which is consistent with methane-associated microbial metabolism acting as the primary mechanism driving the oceanic methane budget (Hanson and Hanson, 1996), where the oxidation of methane results in a decrease of the [CH$_4$] and an enrichment of the heavier isotope (δ^{13}CH$_4$). At the low range of concentrations, the variability in δ^{13}CH$_4$ becomes quite large, suggesting the potential for a variety of inputs or sources to surface values that are near the limit of equilibrium with the atmosphere. The highest methane concentrations with lighter (more negative) isotopic signature were recorded within fresher waters, as shown by the color scale in Fig. 6.
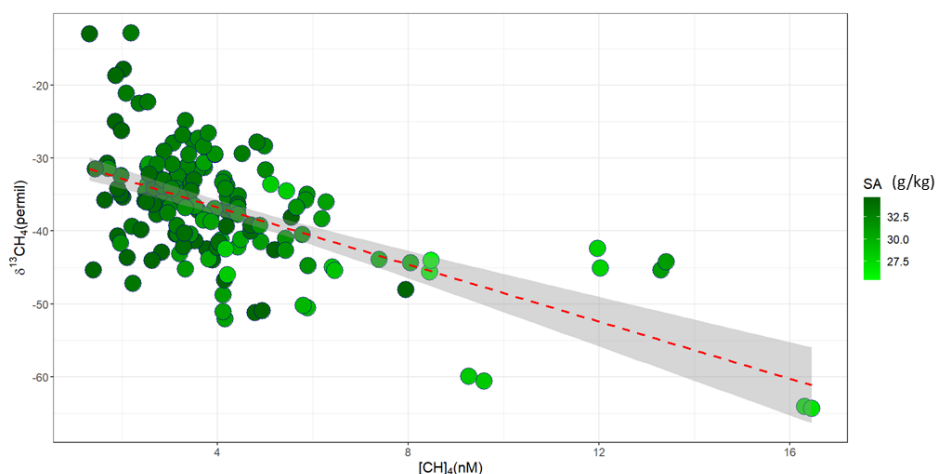
Figure 6: Relationship between the in-situ methane concentrations and the $\delta^{13}C$ isotopic ratio. The red dashed line represents the linear regression (R^2: 0.35). The color scale for the symbols show absolute salinity (SA in g/kg). A shift to higher $\delta^{13}CH_4$ coupled to a decrease in $[CH_4]$ indicates potential microbial oxidation.

3.3 Experimental methane oxidation and production

The microbial oxidation rates (r_{ox}) with rate constants (k_{ox}) were calculated as in Uhlig and Loose (2017), and the values are showed in Table 2.

Table 2: Methane oxidation rate constant ($k_{ox}.av$ (d^{-1})) averaged between the $k_{ox.mass.balance}$ and $k_{ox.isotope.ratio}$, and the microbial methane oxidation rates (r_{ox} (nM/d)). In the table we also show the sample ID, the location (Transect) and the depth of the sample collected; moreover, we show the standard deviation between the averaged k_{ox} (kox.SD). Make the labels in the text consistent with the table.

Sample.ID	Transect	Depth	$k_{ox}.av$ (d^{-1})	$k_{ox}.SD$	r_{ox} (nM/d)
22	JS	609	0.005	0.005	0.997
26	JS	7	0.003	0.001	0.458
36	WNBI	70	0.007	0.005	4.040
37	WNBI	15	0.005	0.002	2.210
39	WNBI	15	0.006	0.000	1.890
40	WNBI	450	0.006	0.001	2.700
41	WNBI	70	0.004	0.002	1.030
43	WNBI	743	0.003	0.002	1.530
45	WNBI	401	0.000	0.000	0.000
58	WC	10	0.010	0.000	3.530
59	WC	10	0.008	0.004	1.690
76	PRS	25	0.000	0.000	0.000

15

78	PRS	25	0.000	0.000	0.000
79	CB	7	0.010	0.001	3.830
81	CB	241	0.009	0.007	1.090
82	CB	241	0.007	0.008	0.436
83	CB	7	0.008	0.008	0.605

482

483   Figure 7 shows the vertical distribution of the averaged methane oxidation rate constants ($k_{ox.mass.balance}$ and

484    $k_{ox.isotope.ratio}$). The vertical trend of the methane oxidation rates showed widespread oxidation potential for

485   methane, with higher values within the shallower waters ($k_{ox.av}$ = 0.01 d^{-1} in WC and CB ~10m depth),

486   followed by $k_{ox.av}$ = 0.009 d^{-1} at 241 m depth in Croker. Both the oxidation rate constants ($k_{ox.mass.balance}$ and

487    $k_{ox.isotope.ratio}$) fell in the range of values between 0 and 0.01 d^{-1}. Positive values of $k_{ox.mass.balance}$ and $k_{ox.isotope.ratio}$

488   indicated a decrease in methane concentrations and an enrichment of ^{13}C; conversely, negative values

489   indicated methane production.

490
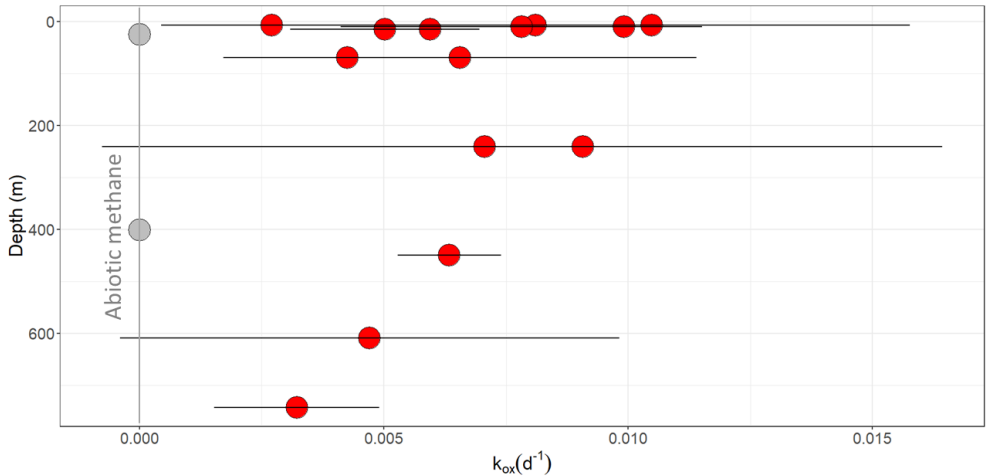
491

492   Figure 7: Vertical profiles of averaged methane oxidation rates constants for mass balance and isotope ratio.

493   The grey dot indicates the samples showing abiotic methane, while the line at 0 determined the area with

494   no microbial methane metabolism. The data > 0 (d^{-1}) suggested methane oxidation potential.

495

496   In summary, the waters of the CAA exhibited a net oxidative environment, in the summer of 2019. The

497   oxidation detection limit was passed between 5 and 18 incubation days after incubation began, revealing

498   the range of rates we observed. The samples with incubation time less than 6 days showed potential change,

499   however, the tight range of time did not allow us to determine a factor for the detection limit.

500

501   **3.4 Microbial community composition**

502   The 16S rRNA gene analyses on the in-situ water column community revealed phylogenetic diversity. The

503   microbial community structure of the water column was predominantly photoautotrophic, but with a high

504   abundance of Flavobacteriaceae, *Polaribacter sp*. (Gonzalez et al., 2008) which can be heterotrophic,

505   psychrophilic, and mesophilic. After the incubation period, the majority of the 16S rRNA gene sequences

506 clustered into OTUs which were taxonomically affiliated with Alphaproteobacteria, Gammaproteobacteria
507 and again Flavobacteriaceae (Bacteroidetes). The dominant taxa occurring in the samples showing methane
508 oxidation were *Oleispira* (γ-proteobacteria), *Planctomarina* (α-proteobacteria),
509 and *Aurantivirga* (flavobacteria, Song et al., 2015). Alphaproteobacteria and Gammaproteobacteria
510 include known MOB, however, *Oleispira* and *Planctomarina* are not yet classified as such. Nevertheless,
511 these taxa were found in Arctic methane incubations by Uhlig et al. (2018), and Gründger et al. (2021), and
512 are therefore likely associated with methane oxidation. The Flavobacteria are known to be secondary
513 consumers of methane, oil, or cellular decay products (Redmond & Valentine, 2012). In particular,
514 Flavobacterium *Polaribacter sp.* is RuBisCO-lacking and the study from Alonso-Sáez et al. (2010) showed
515 that heterotrophic CO_2 assimilation was active within the nutrient-depleted stationary phase conditions in
516 Arctic Sea waters (DeLorenzo et al., 2012). Usually, methane oxidizers have limited ability to consume
517 multi-carbon substrates (Hanson & Hanson, 1996), and many oil degraders have no ability to consume
518 methane (Rojo, 2009). Flavobacteria were often associated with the degradation of high molecular weight
519 dissolved organic carbon compounds (Cottrell and Kirchman, 2000), which may be coincidently associated
520 with methane production (see methane paradox described above, section 1). In almost all the incubations
521 there was occurrence of Chloroplast genome. Summarizing, our dataset emphasized the occurrence
522 of Chloroplast genome, *Oleispira*, *Planctomarina*, and *Aurantivirga* in the methane oxidations (similar
523 outcome of Uhlig et al., 2018 and Gründger et al., 2021). However, little is still known about this
524 relationship, stimulating open questions on the drivers of methane oxidation activity in the Arctic Ocean.
525

526 **3.5 Dissolved methane and isotope ratio in sea ice cores**
527 Methane dissolved in sea ice stayed in the range of 3.3 and 24 nM, showing concentrations a bit higher than
528 in seawater ([CH_4] max in CB = 17nM). The methane maxima were recorded within Westernmost Station
529 sea ice core (24nM), however, all the samples exhibited methane oversaturation with respect to the
530 atmospheric concentration (av. 4.7±0.01 nM) along their profiles. Core 1 at the surface and Core 2 at the
531 bottom (Fig. 8) showed a weak deficit of methane (3.3 and 4.5 nM, respectively), whereas all other data
532 recorded methane supersaturation with respect of atmospheric capacity. The calculation of the
533 concentration of methane sea water at equilibrium with the normal atmosphere was derived by the Bunsen
534 solubility coefficients, using in-situ potential temperature and a constant value of 2 for practical salinity.
535 Core 1 and Core 2 were characterized by thicker multi-year ice (Canadian Ice Service), Core 2 was sampled
536 in the proximity of the Westernmost station. Cores 3, 4, and 5 were collected respectively in Peel Sound,
537 close to Cunningham River, and in Prince Regent Sound (see Fig.1), and they were characterized by first-
538 year ice. In this study, we did not analyze the characteristics of the sea ice (e.g., permeability), which could
539 be used as an indicator of the methane distribution (Verdugo et al., 2021), however, according to its physical
540 and chemical parameters, we were able to identify the role the sea ice played on the methane cycle. Core 2
541 was oversaturated for methane up to 95cm (av. 6.86 ± 1.76 nM), below which showed undersaturation with
542 respect to the methane atmospheric concentration (Fig. 8). The seawater [CH_4] profile showed similar
543 values and similar trend, with oversaturation within the top layers and undersaturation below 75m depth.
544 In Peel Sound the sea ice was characterized by nilas and thin first-year ice and surface water showed similar
545 [CH_4] and $\delta^{13}CH_4$ (11 and 9 nM respectively in sea ice and seawater, and -50 ‰ in both). In Prince Regent
546 Sound the sea ice was constituted by nilas and thick first-year ice (> 120 cm), and [CH_4] assessed the same
547 value in both surface water and sea ice (~7nM), while the isotope ratio measured slightly higher values in
548 the sea ice (~-50 ‰ in surface water and ~-42‰ in sea ice).

549

550
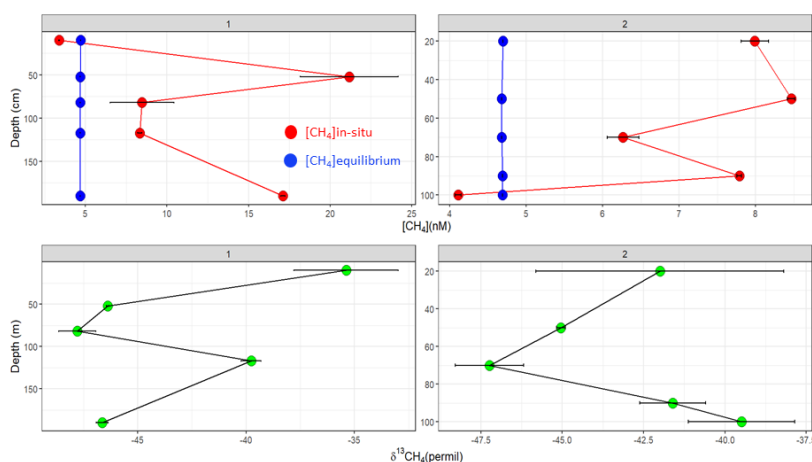
Figure 8: Methane concentrations and isotope ratios along the vertical profiles within sea ice. The red dots indicated the in-situ methane concentrations along the sea ice core, with the methane concentrations at the equilibrium relative to the atmosphere capacity (blue dots). The green dots showed the isotope ratio ($\delta^{13}CH_4$) of cores 1 and 2. The headers displayed the core numbers.

Summarizing, the $\delta^{13}C$ isotopic signature in ice cores was between -52 and -33 ‰, showing shorter variability in comparison to the in-situ water samples data.

4. Discussion

In the Canadian Arctic Archipelago waters, the dissolved methane showed a vertical stratification with methane excess mostly recorded in shallow waters. Here, we also recorded higher methane microbial oxidation rates, likely associated with Pacific-origin microbes and with the seasonal biology. Observing these results in a hydrographic contest, will elucidate about the major drivers of the methane metabolism in this specific region of the Arctic, during the summer.

4.1 The methane oxidation rates across the CAA.

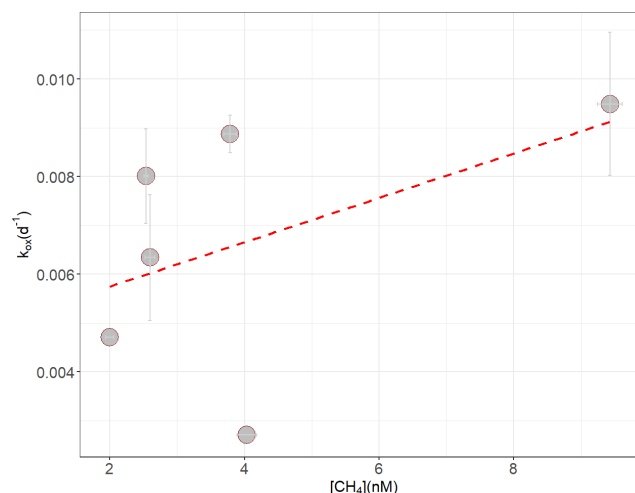The average value of the oxidation rate constant from this study was 0.005±0.003 d^{-1}. Overall, the range of values of k_{ox} and r_{ox} (describing the activity of methane-oxidizing microorganisms, Tab. 2) mainly stayed within the range of values from previous Arctic research (Mau et al., 2017; Uhlig and Loose, 2017). Moreover, the values of r_{ox} showed good fit with global methane data within a broader context (Fig. S2). The only methane oxidations data available from the CAA waters dated back to 2005 (Kitidis et al., 2010) and showed significantly higher k_{ox} values than any other measurements in the Arctic, including near seeps, k_{ox} averaged in Kitidis et al. (2010) is 0.912 d^{-1}. We note that the two oxidation rate measurements of Kitidis et al., were made using methane mass balance alone, which can be subject to high oxidation rate aberrations if methane gas leaks from the incubation chamber.

Previous studies from the Arctic and cold seeps from continental slopes across the globe (Mau et al. 2013; Boetius & Wenzhöfer, 2013) reported elevated methane oxidation activity in marine environments, coincident with high CH_4 concentrations, suggesting that MOB may be able to rapidly increase oxidation rates in response to the food source abundance. However recent studies developed in proximity of methane

580   sources, such as the Arctic shelf gas seeps (Steinle et al. 2015, 2017; Gründger et al., 2021) showed that
581   methane oxidation rates are sometimes mitigated by the seasonal variations of the hydrographical regimes,
582   which trigger a system-wide switch of the efficiency of water column methane oxidizers. In our study, we
583   detected higher microbial methane oxidation rates within the upper 200 m depth (see Fig.7), mainly
584   distributed in shallow waters, with high methane concentrations (Fig. 9). The data measured in CB heavily
585   influences the regression line trend in Figure 10 (R^2: 0.03, p-value: 0.34), as it recorded the highest value
586   of dissolved [CH_4] coupled with high methane oxidation rates. Our results overall corroborated the thesis
587   that methane oxidation is related to methane concentrations. We acknowledge the low amount of data
588   available for coupled in-situ and experimental samples; however, the spatial coverage of these data is
589   presently the best-available record of methane metabolism in the CAA waters.

590

591

592   Figure 9: Methane dissolved in the water column against the averaged methane oxidation rate constants
593   (k_{ox}). The red dashed line indicated the linear regression between the data R^2: 0.03, p-value: 0.34). The
594   labels over the dots indicate the stations (Croker Bay, Wellington Channel, West Navy Board Inlet, Jones
595   Sound).

596

597   To have a wider overview of the relationship between methane concentrations and oxidations, in Figure 10
598   we have aggregated in-situ methane and methane oxidation rate constants from several studies in both
599   enriched and depleted methane environments (including this one). We have plotted the study-average of
600   dissolved methane (in $\log_{10}$ scale) and its oxidation rate constant. These include data from the Gulf of
601   Mexico (GoM), collected directly after the DWH oil spill in 2010 (Kessler et al., 2011; Rogener et al.,
602   2018). As expected, dissolved methane in Gulf of Mexico waters was higher than Arctic waters, however,
603   the methane oxidation rate constant was only slightly higher than the Arctic data. The methane oxidation
604   rate constants do not appear to scale proportionately with the dissolved concentrations. Instead, the plot
605   displayed relatively high [CH_4] associated to low k_{ox} and vice versa. This was also confirmed by the
606   Michaelis-Menten kinetics (Button, 2010; Michaelis–Menten, 1913) (Fig. 10 right box). The result
607   highlights that the kinetics increased hyperbolically with substrate concentration but leveled off once the

608   metabolic pathway was saturated with substrate, the maximum rate achieved by the system was recorded
609   on a value of ~20 nM [CH_4]. The Michaelis-Menten curve was generated excluding the GoM and Kitidis
610   data, because the high values did not allow the convergence. Overall, our values of $k_{ox.}$ were in the low
611   range of Arctic literature values, with an average of 0.006±0.002 d^{-1} (Fig. 10) and showed a great difference
612   in magnitude with the only comparison in the same study area (Kitidis et al., 2010 with averaged k_{ox} of 0.9
613   d^{-1}). Conversely, the dissolved methane concentrations showed close values to Kitidis et al. (2010). The
614   differences in the oxidation rate constant may be due to, a) the nature of the samples (melt-pond and under-
615   ice waters, while we analyzed the entire water column), b) the number of the samples incubated for methane
616   oxidation rates (2 in total, while we had 60 incubations), c) the method used to assess the microbial methane
617   oxidation rate (using exclusively the mass balance, while we also analyzed the isotopic ratio and verified
618   the bags against leaks), d) the changes to the CAA that have taken place between the expeditions (2005 vs
619   2019). Kitidis k_{ox} value was even higher than the values measured in the Gulf of Mexico waters after the
620   Deepwater Horizon (DWH) oil spill in April 2010 (Kessler et al., 2011; Rogener et al., 2018) (see Fig. 10).
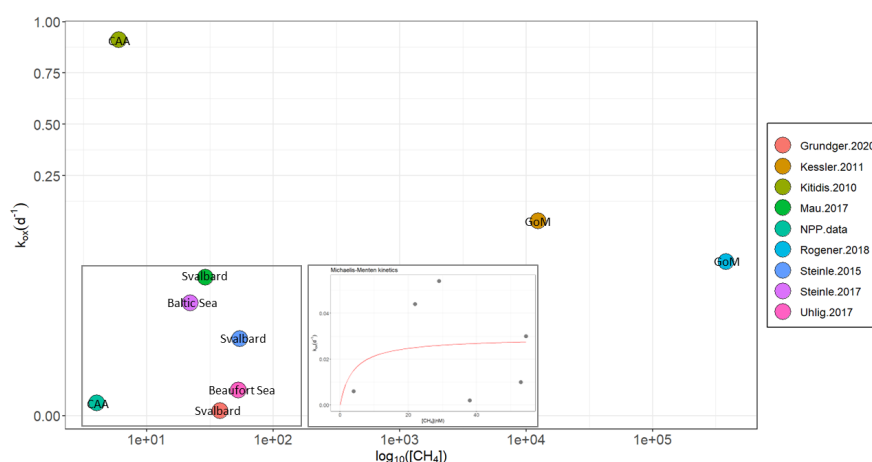
621

622

623   Figure 10: Averaged methane concentrations (in log_{10} scale) and oxidation rate constant from literature. In
624   the figure, we show methane data (both in-situ and oxidation rate constant) from six studies conducted in
625   the Arctic waters, one in the Baltic Sea, and two in the Gulf of Mexico (GoM) waters, after the Deepwater
626   Horizon oil spill in 2010. The labels on the dots indicate the study areas. Kessler et al. (2011) show the
627   values of k_{ox} recorded right after the Deepwater Horizon oil spill in 2010 (Apr–Sept), while the data showed
628   by Rogener et al. (2018) account for k_{ox} values measured from May 2010 to June 2015. Steinle et al. (2015)
629   show methane data from a cold-seep system influenced by gas hydrates along the Svalbard continental
630   margin, in August 2011 and 2012; whereas Steinle et al. (2017) investigated the methane concentrations
631   and oxidations in seasonally hypoxic environments (Eckernförde Bay in the SW Baltic Sea), between
632   October 2012 and September 2014. Grundger et al. (2020) measured dissolved methane and its oxidation
633   rate constants at the shallow shelf of Prins Karls Forlan (Arctic shelf) in the Spring and Summer between
634   2015 and 2017. Mau et al. (2013) show methane data from a seepage area of Svalbard, extending from 74°
635   to 79°N. Uhlig et al (2018) show methane data from the Beaufort Sea; and finally, Kitidis et al (2010) and
636   the NPP data are data measured from the CAA waters. Mau et al. (2017), Steinle et al. (2017), Grundger et
637   al. (2020), Rogener et al. (2018), and Kessler et al. (2011) measured methane oxidation rates derived from

638   tracer incubations using ^{3}H-CH$_4$. Our study and Uhlig et at (2018) used stable isotopes instead and measured
639   both methane concentrations and isotope ratio. The x and y axis are expressed in log$_{10}$ scale, in order to
640   scale the different values. The grey boxes highlight the data following the Michaelis-Menten kinetics (plot
641   window on the right).

642

643   **4.2 Methane oxidation rates in oversaturated waters.**
644   The methane oversaturation in seawater, with respect to the atmospheric concentrations, recorded the
645   highest magnitudes in shallow Crocker Bay (17.7nM), Barrow East (14.4 nM), and Peel Sound (9.13 nM)
646   waters, two of the three stations were located in the western part of the transect (with longitudes > 90 ⁰W).
647   Croker Bay, despite being located at 83 ⁰W, was non-representative of the eastern Channel, because of its
648   influence from the Devon Ice Cap drainage (D'Angelo et al., 2022). Barrow East and Peel Sound waters
649   were characterized respectively by high watershed supply provided by Cunningham and Garnier Rivers
650   (corroborated by McLaughlin et al., 2014), and by the watershed drainage of the marine-terminating rivers
651   from the southern CAA (Brown et al., 2020). All three sites were characterized by high meltwater input
652   (with MW and SIM > 10%) and detrital organic matter supply, supporting high rates of biological
653   productivity (chlorophyll-α fluorescence and nutrients data: https://doi.org/10.18739/A2BN9X45M).
654   Methanogenesis in the terrestrial fluvial systems and beneath terrestrial glaciers could explain the high
655   marine CH$_4$ concentrations observed at these sites (Bange et al., 2010; Valentine, 2011). The isotopic
656   signature of methane in shallow Croker Bay waters reached values < - 64 ‰ (very depleted in δ^{13}C),
657   suggesting subglacial methanogenesis (Pain et al., 2020) from the Devon Ice Cap runoff. We did not have
658   incubation results from Barrow East and Peel Sound; however, we recorded methane oxidation potential in
659   Croker Bay. In this site, the incubation results showed microbial methane oxidation potential in both surface
660   and deeper layers (av. k_{ox} at surface = 0.009 ± 0.002 d^{-1}, av. k_{ox} at 241m depth = 0.008±0.001 d^{-1}, see
661   Fig.10), suggesting that the methane dissolved in the water column could be oxidized before reaching the
662   atmosphere.

663

664   **4.3 Hydrography influencing the methane budget**
665   To have additional insights into the role of the meltwater influencing the biogeochemistry in waters
666   proximate to meltwater runoff, we observed the linearity between the methane data (both in-situ and ex-
667   situ) and the freshwaters (Fig. 11). Overall, methane oxidation rates showed direct correlation with
668   freshwater masses, suggesting the influence of the CAA meltwater runoff on the methane metabolism. This
669   correlation does not include data CB, due to an artifact of the δ^{18}O interpolation in the MP, see D'Angelo
670   et al, (2022) (https://doi.org/10.5194/essd-2022-306), where we recorded the highest freshwater signal for
671   oxygen isotopes, triggered by the glacial runoff of Devon Ice Cap; hence, slightly stronger correlations
672   between the methane data and the MW are expected. This outcome is somewhat at odds with a previous
673   study conducted in the CAA (i.e., Manning et al., 2022), which showed that rivers (included in what we
674   define meteoric waters) were not a significant source of CH$_4$ to the Arctic Ocean from early July to mid-
675   October in years 2015-2018. Here, we did not measure the CH4 concentration within the riverine systems,
676   so we cannot compute the flux. Nevertheless, we observe a consistent positive correlation between marine
677   [CH4] and freshwater distribution. This discrepancy motivates future field campaigns in the Canadian
678   Arctic Archipelago, with high spatial and temporal resolution mapping immediately before, during and
679   after ice melt.

680
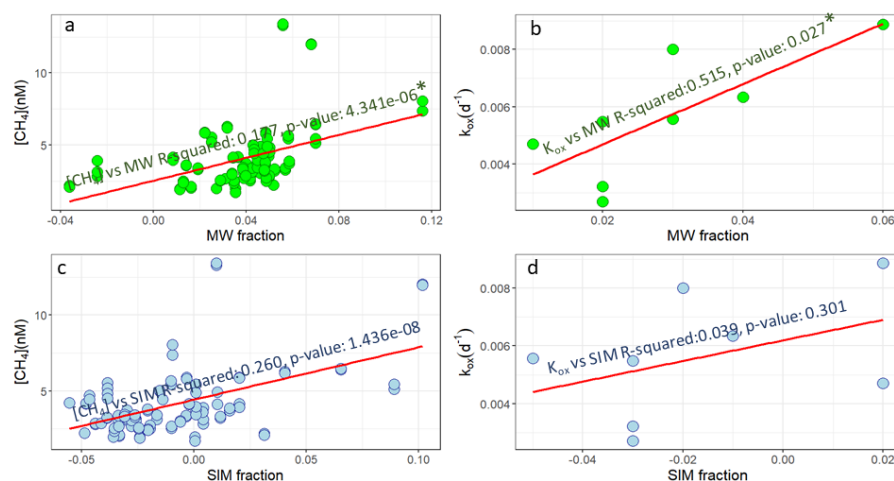
Figure 11: In-situ methane concentrations, and averaged methane oxidation rate constants (k_{ox}) in correlation with MP results. Panels (a) and (c) show methane in-situ concentrations against the meltwater masses, sea ice, and meteoric meltwaters (SIM and MW); panels (b) and (d) display the methane oxidation rate constant in relation to the meltwaters. * The results of MW potentially undergo increase, as they did not include the freshwater supply from Devon Ice Cap.

Expanding the correlations within the Pacific and Atlantic waters, dissolved methane was inversely correlated to AW (-0.4 Spearman's rank) and positively correlated with PW (0.3 Spearman's rank) (see Fig. S3). This resulted a bimodal distribution of methane across the study area (Fig. 12). Methane oxidation occurred in Pacific-dominating stations, showing an inverse correlation with AW (-0.17 Spearman's rank). In the Atlantic water regime, dissolved methane was depleted with concentrations below the equilibrium saturation range, and we recorded weaker methane microbial metabolism. The occurrence of no detectable methane oxidation in the deep layers of West Navy Board Inlet and in shallow Prince Regent Sound waters was not associated to unique thermohaline characteristics of the two sites, and unfortunately, the community structure was not analyzed in those sites.
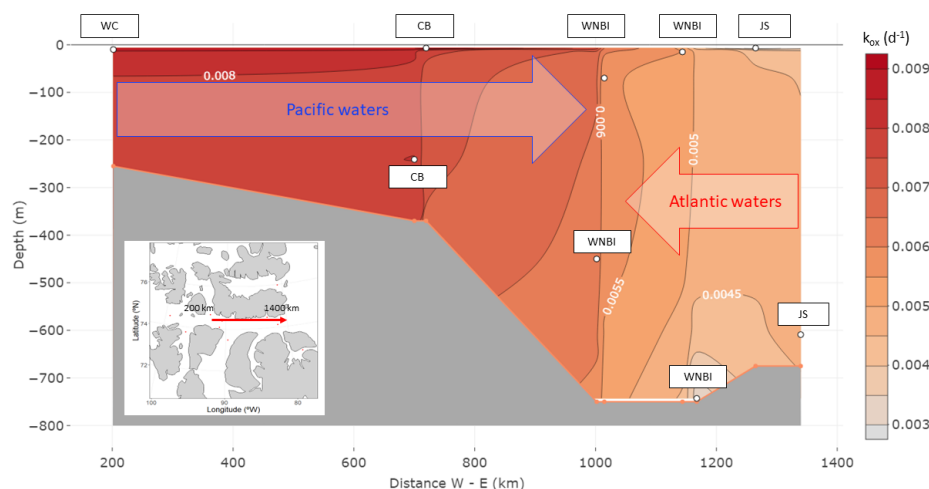
Figure 12: Section of the Parry Channel with color scale showing the k_{ox} averaged by transect and depth. Here we show the $k_{ox}>0$, excluding potential production signal in Western-most Station. The arrows indicate the AW and PW intruding into the channel. The white dots describe the data points, while the text boxes on top display the locations. The x axis displays the distances (in km) from the Wellington Channel 200 km (Longitude = 93.1071 ⁰W) to the most eastern location 1400 km (Longitude = 78.2579 ⁰W), see details in the map in the bottom corner.

In summary, we found weak methane metabolism in AW, while it was stronger in meltwaters and PW, with higher microbial oxidation rates and weak signal of methane potential production. These results tend to support the role of surface processes in the CAA, including meltwater and biological production as significantly associated with excess methane and higher methane oxidation, above all in the melt season (e.g., estuarine circulation). The overall picture suggested supersaturation of in-situ methane in shallow waters, coupled with faster oxidation rates in meltwater and Pacific regime, speculating prevention of the methane migration into the atmosphere towards the western CAA.

4.4 Sea Ice influence on the methane budget in the CAA.

The Western CAA contained the greatest sea ice cover, mostly as multi-year ice (MYI, see Fig. 13). Further, the satellite-derived sea ice cover and the water mass estimates of sea ice meltwater tended to coincide with greatest contributions in the West, with >10% occupying the water volume (D'Angelo et al., 2022, https://doi.org/10.5194/essd-2022-306). The fluorescence data and the phytoplanktonic community data (provided by the Menden-Deuer lab, URI-GSO), strongly indicated that on this side of the Channel there was a time lag with the Eastern Sound, showing a delay in the phytoplankton bloom. This phenomenon could have affected the methane distribution within the area, as spring blooms could activate methanotrophs and methanogens metabolism. In WS, the maximum value of dissolved methane reached 8.7nM at 5m depth, whereas the $\delta^{13}C$ isotopic ratio showed very enriched values (reaching -13 ‰ at the subsurface layers), suggesting a marine source of methane due to the preferred microbial use of ^{12}C. The microbial methane oxidation showed higher rates in the northern Sound, with the minima in ice-covered sites (Fig. 13). This result highlighted a methane-metabolic separation between the ice-covered and open-water

727   Channel. Increased ice permeability at the ice bottom triggers methane release, causing low methane
728   concentrations at the bottom of the ice and methane enrichment in the water underneath (Verdugo et al.,
729   2021; Damm et al., 2015). This behavior was detected in the methane profile within Core 2 (collected close
730   to the Western-most station). Here, the sea ice enriched in methane could have released the gas and the
731   relict detritus, favoring the conditions for microbial methane production, explaining the methane deficit in
732   the ice bottom and the methane excess in the waters underneath. The same condition, but backwards, was
733   recorded in Core 1, where we recorded sea ice oversaturated in methane, with the top centimeters showing
734   methane deficit. The methane initially entrapped in the sea ice was probably released into the atmosphere
735   when the sea ice surface became permeable (Verdugo et al., 2021). Summarizing, the sea ice influenced the
736   methane cycle in our samples, triggering the methane metabolism towards the West. Comparing our results
737   with the ones from previous studies in the same location (Kitidis et al., 2010), sea ice similarly influenced
738   the methane oxidation rates (SIM and k_{ox} correlation = 0.63 Spearman's rank). Our outcome, confirmed by
739   previous studies conducted in Utqiagvik and the Central Arctic (Loose et al., 2011; Damm et al., 2015;
740   Damm et al., 2018), suggested that the residence time of methane gas in sea ice could allow it to accumulate
741   during the freezing period and be released during the melt period, supporting the metabolic consumption in
742   SIM. In conclusion, we can state that the sea ice in the CAA is defined by a bimodal distribution of marine
743   methane. In the past, other studies showed the correlation between the sea ice and the greenhouse gases in
744   the Arctic Ocean during the summer (Damm et al., 2018, Verdugo et al., 2021), however, no data were yet
745   referred to our study area.

746
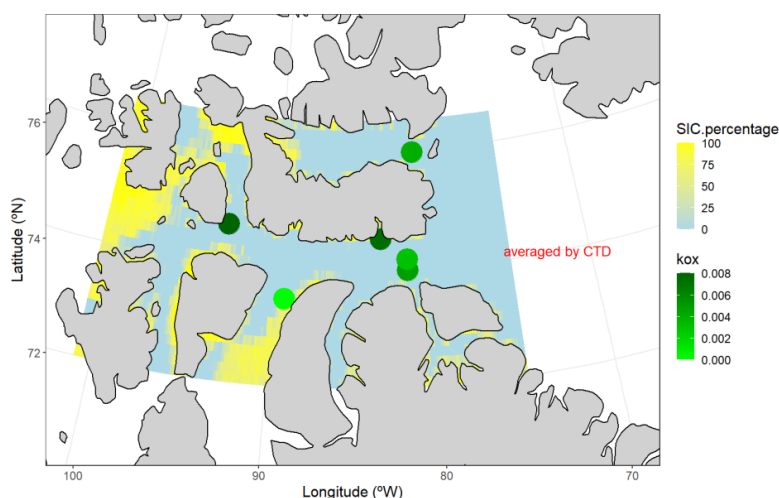
748   Figure 13: top view maps of the study area, with raster plots of the sea ice concentrations, and scatter plot
749   showing k_{ox}. averaged by CTD. The color scales show the SIC percentage and the k_{ox} values (d^{-1}).

750

4.5 Marine microbial communities driving the methane cycle in the CAA.
752   The genomic community composition results highlighted *Oleispira*, *Planctomarina* and *Aurantivirga*
753   occurrence in our samples in which methane oxidation was detected, suggesting these could be the methane-

754 oxidizing taxa responsible of the methane consumption in the CAA. Furthermore, the Chloroplast genome
755 occurred in the methane-oxidated shallow samples. In Uhlig et al. (2018), *Oleispira* was also very abundant
756 in the long-incubation samples compared to very low abundances in the in-situ samples, mainly dominated
757 by α- and γ- proteobacteria. Here, after incubating the samples with the methane standard, the communities
758 shifted toward higher fractions of γ-proteobacteria over time. From our analysis, we detected the shift
759 toward α-proteobacteria instead, with *Planctomarina* dominance. The occurrence of *Oleispira* (likely
760 belonging to *Oleispira lenta,* Wang et al., 2012) and *Aurantivirga* taxa highlighted the influence of the PW
761 in the methane oxidation, as these taxa have been found predominantly in the North Pacific waters (Wang
762 et al., 2012; Song et al., 2015). In particular, *Aurantivirga* occurred strictly within the bottom layer
763 characterized by high turbidity, confirming its association with sediments. Our potential methane oxidations
764 occurred all within waters enriched with detrital material (corroborated by the turbidity data, reaching for
765 example 0.37 NTU in CB), supplied by the meltwater runoff. Along the water column, the Chloroplast ge.
766 occupied the shallow layers, mainly towards the West. This confirmed the late bloom as aforementioned.
767 This result could confirm the hypothesis of the methane production in surface waters through the P redox
768 pathways in phosphate-starved environments (Karl et al., 2008; Repeta et al., 2016; Sosa et al., 2017 and
769 2020), also corroborated by the inverse correlation of -0.40 between the dissolved $[CH_4]$ and the $[PO]_4^{3-}$ in
770 the Spearman's rank. Concluding, the dominant taxa associated to our oxidations are not known MOB, but
771 they have been recently connected to the methane metabolism, posing the baseline for further
772 investigations.
773

5. Conclusions

775 Collectively, the CAA waters showed methane oversaturation with respect to atmospheric saturation
776 capacity in the upper layers. The methane oversaturation was mainly associated with the meltwaters and
777 primary production (in nutrient depleted environments), likely following the Methylphosphonate (MPn)
778 esters metabolization, as explained in Repeta et al. (2016) and Sousa et al. (2020). The CAA waters were
779 characterized by methane oxidizers, with 74% showing potential methane oxidation, 5% showing potential
780 production, and 21% resulting methane abiotic (over 17 samples). The fastest oxidation rates were recorded
781 within meltwaters and Pacific-origin Waters, however the k_{ox} showed lower rates than the k_{ox} measured
782 during a cruise held in 2005 in the CAA (Kitidis et al., 2010). The community structure likely responsible
783 for the methane oxidation was characterized by three main groups nonbelonging to known MOB, but
784 recently associated with the methane metabolism (*Aurantivirga, Oleispira and Planktomarina*);
785 *Aurantivirga* and *Oleispira* were both isolated from PWs. This outcome suggested that the PW
786 predominance of the CAA waters could define hotspots for methane oxidations. The ice-covered site
787 showed the lowest methane oxidation rates, suggesting potential methane production, likely due to the late
788 phytoplankton bloom, delayed by the sea ice coverage. This data strengthened the hypothesis that the sea
789 ice acted as a barrier for the gas exchange, defining the underneath water's hotspot for methane excess
790 during the summer. The Pacific regime of the CAA was characterized by methane oxidizers predominance
791 and exhibited high potential oxidation rates.
792 Summarizing, the sea ice would potentially trigger methane production, the Pacific and melt waters would
793 enhance methanotrophy, while the Atlantic Waters would be mostly methane abiotic. We could divide the
794 entire study area into four environments, according to the methane distribution: (a) sea ice, with methane
795 excess; (b) meltwaters (meteoric and sea ice melt), characterized by methane oxidations in oversaturated
796 waters; (c) Pacific waters, with high methane oxidation rates, likely due to methanotrophs; (d) Atlantic
797 regime, mostly abiotic for methane. Due to the Atlantification of the Arctic Ocean (Polyakov et al., 2017,

798   2020), we would expect higher intrusion of AW in the CAA at the expense of PW, with consequent sea ice
799   melting. According to our outcome, the takeaway is that in such a scenario, we would expect stronger
800   stratification, with methane excess alternated to microbial oxidations at the top 200m, overlaying methane-
801   depleted waters, with reduced methane oxidation rates.
802

Data availability

804   The produced database of this study has been archived in Arctic Data Center and can be assessed using the
805   following link: https://doi.org/10.18739/A2BN9X45M.
806

Author contribution

808   B.L. designed the research. B.L. and A.D. implemented the study. A.D., C.G-E., Z.K., J.S., F.C., N.V.,
809   H.R., T.E., S.U., B.L., were involved in the sampling activities. A.D., B.L., N.V., H.R., T.E., S.U.,
810   performed the analysis. A.D., B.L., A.L.K., M.G-M., F.C., C.G-E. processed the data. A.D. and B.L. wrote
811   the manuscript, with input from all authors. The authors declare that they have no conflict of interest.
812

Competing interests

814   The authors declare that they have no conflict of interest.
815

References

829 Agnew, T. and Howell, S.: The use of operational ice charts for evaluating passive microwave ice
830 concentration data, Atmosphere - Ocean, 41, 317–331, https://doi.org/10.3137/ao.410405, 2003.

831 Alonso-Sáez, L., Galand, P. E., Casamayor, E. O., Pedrós-Alió, C., and Bertilsson, S.: High bicarbonate
832 assimilation in the dark by Arctic bacteria, ISME Journal, 4, 1581–1590,
833 https://doi.org/10.1038/ismej.2010.69, 2010.

834 Anthony, C. (1982) The Biochemistry of Methylotrophs. London, UK: Academic Press.

835 Bange, H. W., Freing, A., Kock, A., & Löscher, C. R. (2010). Marine pathways to nitrous oxide. In Nitrous
836 Oxide and Climate Change (1st ed., pp. 36–62). Routledge. https://doi.org/10.4324/9781849775113

837 Bhatia, M. P., Waterman, S., Burgess, D. O., Williams, P. L., Bundy, R. M., Mellett, T., Roberts, M., and
838 Bertrand, E. M.: Glaciers and Nutrients in the Canadian Arctic Archipelago Marine System, Global
839 Biogeochem Cycles, 35, https://doi.org/10.1029/2021GB006976, 2021.

840 Boden, Rich, et al. "Novel Methylotrophic Bacteria Isolated From the River Thames (London, UK)."
841 Environmental Microbiology, vol. 10, no. 12, 2008, pp. 3225-36.

842 Boetius, A. and Wenzhöfer, F.: Seafloor oxygen consumption fuelled by methane from cold seeps,
843 https://doi.org/10.1038/ngeo1926, September 2013.

844 Brown, K. A., Williams, W. J., Carmack, E. C., Fiske, G., François, R., McLennan, D., and Peucker-
845 Ehrenbrink, B.: Geochemistry of Small Canadian Arctic Rivers with Diverse Geological and Hydrological
846 Settings, J Geophys Res Biogeosci, 125, https://doi.org/10.1029/2019JG005414, 2020.

847 Brusseau, G. A., Tsien, H.-C., Hanson, R. S., and Wackett, L. P.: Optimization of trichloroethylene
848 oxidation by methanotrophs and the use of a colorimetric assay to detect soluble methane monooxygenase
849 activity, Biodegradation, Kluwer Academic Publishers, 19–29 pp., 1990.

850 Carmack, E. C., Yamamoto-Kawai, M., Haine, T. W. N., Bacon, S., Bluhm, B. A., Lique, C., Melling, H.,
851 Polyakov, I. v., Straneo, F., Timmermans, M. L., and Williams, W. J.: Freshwater and its role in the Arctic
852 Marine System: Sources, disposition, storage, export, and physical and biogeochemical consequences in
853 the Arctic and global oceans, https://doi.org/10.1002/2015JG003140, 1 March 2016.

854 Chistoserdova L. Modularity of methylotrophy, revisited. Environ Microbiol. 2011 Oct;13(10):2603-22.
855 doi: 10.1111/j.1462-2920.2011.02464.x. Epub 2011 Mar 28. PMID: 21443740.

856 Cottrell, M. T. and Kirchman, D. L.: Community Composition of Marine Bacterioplankton Determined by
857 16S rDNA Gene Clone Libraries and Fluorescence In Situ Hybridization, APPLIED AND
858 ENVIRONMENTAL MICROBIOLOGY, 5116–5122 pp., 2000.

859 Cowen, J. P., Wen, X., and Popp, B. N.: PII S0016-7037(02)00975-4 Methane in aging hydrothermal
860 plumes, 2002.

861 Crespo-Medina, M., Twing, K. I., Kubo, M. D. Y., Hoehler, T. M., Cardace, D., WCollom, T., and Schrenk,
862 M. O.: Insights into environmental controls on microbial communities in a continental serpentinite aquifer
863 using a microcosm-based approach, Front Microbiol, 5, https://doi.org/10.3389/fmicb.2014.00604, 2014.

864   D'Angelo, A., Garcia-Eidell, C., Knowlton, C., Gingras, A., Morin, H., Coleman, D., Kaelblein, J.,
865   Raziuddin, H., VanKeersbilck, N., Rivera, T. J., Kopka, K., Boleaga, Y., Estes, K., Nodal, A., Schulze, E.,
866   Ewa, T., Shaban, M., Umar, S., Santana, R., Strock, J., Gruebel, E., Digilio, M., Ludkin, R., Gong, D.,
867   Kerrigan, Z., Otokiak, M., Crable, F., Trenholm, N., Millstone, T., Montenegro, K., Kim, M., Porter, G.,
868   Ketter, T., Berkelhammer, M., King, A. L., Gonzalez-Meler, M. A., and Loose, B.: Water masses
869   distribution in the Canadian Arctic Archipelago: Implementation of the Optimal MultiParameter analysis
870   (OMP), Earth Syst. Sci. Data Discuss. [preprint], https://doi.org/10.5194/essd-2022-306, 2022.

871   Damm, E., Bauch, D., Krumpen, T., Rabe, B., Korhonen, M., Vinogradova, E., and Uhlig, C.: The
872   Transpolar Drift conveys methane from the Siberian Shelf to the central Arctic Ocean, Sci Rep, 8,
873   https://doi.org/10.1038/s41598-018-22801-z, 2018.

874   Damm, E., Helmke, E., Thoms, S., Schauer, U., Nöthig, E., Bakker, K., Kiene, R. P., and Wegener, A.:
875   Methane production in aerobic oligotrophic surface water in the central Arctic Ocean, Biogeosciences,
876   1099–1108 pp., 2010.

877   Damm, E., Kiene, R. P., Schwarz, J., Falck, E., and Dieckmann, G.: Methane cycling in Arctic shelf water
878   and its relationship with phytoplankton biomass and DMSP, Mar Chem, 109, 45–59,
879   https://doi.org/10.1016/j.marchem.2007.12.003, 2008.

880   Damm, E., Rudels, B., Schauer, U., Mau, S., and Dieckmann, G.: Methane excess in Arctic surface water-
881   triggered by sea ice formation and melting, Sci Rep, 5, https://doi.org/10.1038/srep16179, 2015.

882   Dang, H. and Lovell, C. R.: Microbial Surface Colonization and Biofilm Development in Marine
883   Environments, Microbiology and Molecular Biology Reviews, 80, 91–138,
884   https://doi.org/10.1128/mmbr.00037-15, 2016.

885   DeLorenzo, S., Bräuer, S. L., Edgmont, C. A., Herfort, L., Tebo, B. M., and Zuber, P.: Ubiquitous Dissolved
886   Inorganic Carbon Assimilation by Marine Bacteria in the Pacific Northwest Coastal Ocean as Determined
887   by Stable Isotope Probing, PLoS One, 7, https://doi.org/10.1371/journal.pone.0046695, 2012.

888   DiTullio G, Lee P (2019) Dissolved nutrient concentrations, High Arctic Ocean, August-September 2018.
889   Arctic Data Center. https://doi.org/10.18739/A2CN6Z03F

890   Dunbar, Moira. "The Geographical Position of the North Water." *Arctic* 22: 438-441,
891   DOI:10.14430/ARCTIC3235 Corpus ID: 129164760, 1969.

892   Dunfield PF, Yuryev A, Senin P, Smirnova AV, Stott MB, Hou S, Ly B, Saw JH, Zhou Z, Ren Y, Wang J,
893   Mountain BW, Crowe MA, Weatherby TM, Bodelier PL, Liesack W, Feng L, Wang L, Alam M. Methane
894   oxidation by an extremely acidophilic bacterium of the phylum Verrucomicrobia. Nature. 2007 Dec
895   6;450(7171):879-82. doi: 10.1038/nature06411. Epub 2007 Nov 14. PMID: 18004300.

896   Fenwick, L., Capelle, D., Damm, E., Zimmermann, S., Williams, W. J., Vagle, S., and Tortell, P. D.:
897   Methane and nitrous oxide distributions across the North American Arctic Ocean during summer, 2015, J
898   Geophys Res Oceans, 122, 390–412, https://doi.org/10.1002/2016JC012493, 2017.

899   Ferré, B., Jansson, P. G., Moser, M., Serov, P., Portnov, A., Graves, C. A., Panieri, G., Gründger, F., Berndt,
900   C., Lehmann, M. F., and Niemann, H.: Reduced methane seepage from Arctic sediments during cold
901   bottom-water conditions, Nat Geosci, 13, 144–148, https://doi.org/10.1038/s41561-019-0515-3, 2020.

902 Fisher, R. E., Sriskantharajah, S., Lowry, D., Lanoisellé, M., Fowler, C. M. R., James, R. H., Hermansen,
903 O., Lund Myhre, C., Stohl, A., Greinert, J., Nisbet-Jones, P. B. R., Mienert, J., and Nisbet, E. G.: Arctic
904 methane sources: Isotopic evidence for atmospheric inputs, Geophys Res Lett, 38,
905 https://doi.org/10.1029/2011GL049319, 2011.

906 Florez-Leiva, L., Damm, E., and Farías, L.: Methane production induced by dimethylsulfide in surface
907 water of an upwelling ecosystem, Prog Oceanogr, 112–113, 38–48,
908 https://doi.org/10.1016/j.pocean.2013.03.005, 2013.

909 Gonzalez, J.M., Fernandez-Gomez, B., Fernandez-Guerra, A., Gomez-Consarnau, L., Sanchez, O., Coll-
910 Llado, M., Del Campo, J., Escudero, L., Rodriguez-Martinez, R., Alonso-Saez, L., Latasa, M., Paulsen, I.,
911 Nedashkovskaya, O., Lekunberri, I., Pinhassi, J., and Pedros-Alio, C. "Genome analysis of the
912 proteorhodopsin-containing marine bacterium Polaribacter sp. MED152 (Flavobacteria)." Proc. Natl. Acad.
913 Sci. USA (2008) 105:8724-8729.

914 Grant, N. J. and Whiticar, M. J.: Stable carbon isotopic evidence for methane oxidation in plumes above
915 Hydrate Ridge, Cascadia Oregon Margin, Global Biogeochem Cycles, 16, 71-1-71–13,
916 https://doi.org/10.1029/2001gb001851, 2002.

917 Graves, C. A., L. Steinle, G. Rehder, H. Niemann, D. P. Connelly, D. Lowry,R. E. Fisher, A. W. Stott, H.
918 Sahling, andR. H. James (2015), Fluxes and fate ofdissolved methane released at theseafloor at the landward
919 limit of thegas hydrate stability zone offshorewestern Svalbard, J. Geophys. Res.Oceans,120, 6185–6201,
920 doi:10.1002/2015JC011084.

921 Gründger, F., Probandt, D., Knittel, K., Carrier, V., Kalenitchenko, D., Silyakova, A., Serov, P., Ferré, B.,
922 Svenning, M. M., and Niemann, H.: Seasonal shifts of microbial methane oxidation in Arctic shelf waters
923 above gas seeps, Limnol Oceanogr, 66, 1896–1914, https://doi.org/10.1002/lno.11731, 2021.

924 Hanson RS, Hanson TE. Methanotrophic bacteria. Microbiol Rev. 1996 Jun;60(2):439-71. doi:
925 10.1128/mr.60.2.439-471.1996. PMID: 8801441; PMCID: PMC239451.

926 Hoefman S. From nature to nurture: isolation, physiology and preservation of methane-oxidizing bacteria.
927 [Ghent, Belgium]: Ghent University. Faculty of Sciences; 2013.

928 Ingram, R. G. and Larouche, P.: Variability of an under-ice river plume in Hudson Bay, J Geophys Res
929 Oceans, 92, 9541–9547, https://doi.org/10.1029/JC092iC09p09541, 1987.

930 Jakobsson, M., R. Macnab, L. Mayer, R. Anderson, M. Edwards, J. Hatzky, H. W. Schenke, and P. Johnson.
931 An improved bathymetric portrayal of the Arctic Ocean: Implications for ocean modeling and geological,
932 geophysical and oceanographic analyses, Geophysical Research Letters, DOI: 10.1029/2008GL033520,
933 2008.

934 Jensen, S., Neufeld, J. D., Birkeland, N. K., Hovland, M., and Murrell, J. C.: Methane assimilation and
935 trophic interactions with marine Methylomicrobium in deep-water coral reef sediment off the coast of
936 Norway, FEMS Microbiol Ecol, 66, 320–330, https://doi.org/10.1111/j.1574-6941.2008.00575.x, 2008.

937 Karl, D., Beversdorf, L., Björkman, K. et al. Aerobic production of methane in the sea. Nature Geosci 1,
938 473–478 (2008). https://doi.org/10.1038/ngeo234

939 Kessler JD, Valentine DL, Redmond MC, Du M, Chan EW, Mendes SD, Quiroz EW, Villanueva CJ, Shusta
940 SS, Werra LM, Yvon-Lewis SA, Weber TC. A persistent oxygen anomaly reveals the fate of spilled
941 methane in the deep Gulf of Mexico. Science. 2011 Jan 21;331(6015):312-5. doi: 10.1126/science.1199697.
942 Epub 2011 Jan 6. PMID: 21212320.

943 Kitidis, V., Upstill-Goddard, R. C., and Anderson, L. G.: Methane and nitrous oxide in surface water along
944 the   North-West   Passage,   Arctic   Ocean,   Mar   Chem,   121,   80–86,
945 https://doi.org/10.1016/j.marchem.2010.03.006, 2010.

946 Kudela, R. M., Seeyave, S., and Cochlan, W. P.: The role of nutrients in regulation and promotion of
947 harmful   algal   blooms   in   upwelling   systems,   Prog   Oceanogr,   85,   122–135,
948 https://doi.org/10.1016/j.pocean.2010.02.008, 2010.

949 Lenhart, K., Klintzsch, T., Langer, G., Nehrke, G., Bunge, M., Schnell, S., and Keppler, F.: Evidence for
950 methane production by the marine algae Emiliania huxleyi, Biogeosciences, 13, 3163–3174,
951 https://doi.org/10.5194/bg-13-3163-2016, 2016.

952 Loose, B., Schlosser, P., Perovich, D., Ringelberg, D., Ho, D. T., Takahashi, T., Richter-Menge, J.,
953 Reynolds, C. M., Mcgillis, W. R., and Tison, J. L.: Gas diffusion through columnar laboratory sea ice:
954 Implications for mixed-layer ventilation of CO2 in the seasonal ice zone, Tellus B Chem Phys Meteorol,
955 63, 23–39, https://doi.org/10.1111/j.1600-0889.2010.00506.x, 2011.

956 Mahieu, K., Visscher, A. de, Vanrolleghem, P. A., and Cleemput, O. van: Carbon and hydrogen isotope
957 fractionation by microbial methane oxidation: Improved determination, in: Waste Management, 389–398,
958 https://doi.org/10.1016/j.wasman.2005.11.006, 2006.

959 Mau, S., Blees, J., Helmke, E., Niemann, H., and Damm, E.: Vertical distribution of methane oxidation and
960 methanotrophic response to elevated methane concentrations in stratified waters of the Arctic fjord
961 Storfjorden (Svalbard, Norway), Biogeosciences, 10, 6267–6268, https://doi.org/10.5194/bg-10-6267-
962 2013, 2013.

963 Mclaughlin, F., Carmack, E., Proshutinsky, A., Krishfield, R. A., Guay, C., Yamamoto-Kawai, M., Jackson,
964 J. M., and Williams, B.: The Rapid Response of the Canada Basin to Climate Forcing: FROM
965 BELLWETHER   TO   ALARM   BELLS,   Source: Oceanography,   24,   146–159,
966 https://doi.org/10.2307/24861309, 2007.

967 Oh, Y., Zhuang, Q., Liu, L., Welp, L. R., Lau, M. C. Y., Onstott, T. C., Medvigy, D., Bruhwiler, L.,
968 Dlugokencky, E. J., Hugelius, G., D'Imperio, L., and Elberling, B.: Reduced net methane emissions due to
969 microbial   methane   oxidation   in   a   warmer   Arctic,   Nat   Clim   Chang,   10,   317–321,
970 https://doi.org/10.1038/s41558-020-0734-z, 2020.

971 Pachauri, R. K., Mayer, Leo., and Intergovernmental Panel on Climate Change: Climate change 2014 :
972 synthesis report, 151 pp., n.d.

973 Poehlein, A., Solano, J. D. M., Flitsch, S. K., Krabben, P., Winzer, K., Reid, S. J., Jones, D. T., Green, E.,
974 Minton, N. P., Daniel, R., and Dürre, P.: Microbial solvent formation revisited by comparative genome
975 analysis, Biotechnol Biofuels, 10, https://doi.org/10.1186/s13068-017-0742-z, 2017.

976   Pol A, Heijmans K, Harhangi HR, Tedesco D, Jetten MS, Op den Camp HJ. Methanotrophy below pH 1
977   by a new Verrucomicrobia species. Nature. 2007 Dec 6;450(7171):874-8. doi: 10.1038/nature06222. Epub
978   2007 Nov 14. PMID: 18004305.

979   Polyakov, I. V., Alkire, M. B., Bluhm, B. A., Brown,K. A., Carmack, E. C., Chierici,
980   M., Danielson, S. L.,Ellingsen, I., Ershova, E. A., Gårdfeldt, K., Ingvaldsen, R.B., Pnyushkov, A.
981   V., Slagstad, D., and Wassmann, P.: Bo-realization of the Arctic Ocean in Response to
982   AnomalousAdvection From Sub-Arctic Seas, Front. Mar. Sci., 7,
983   491,https://doi.org/10.3389/fmars.2020.00491, 2020.

984   Polyakov, I. V., Pnyushkov, A. V., Alkire, M. B., Ashik, I. M., Bau-mann, T. M., Carmack, E. C.,
985   Goszczko, I., Guthrie, J., Ivanov, V.V., Kanzow, T., Krishfield, R., Kwok, R., Sundfjord, A., Morison,J.,
986   Rember, R., and Yulin, A.: Greater role for Atlantic inflows onsea-ice loss in the Eurasian Basin of the
987   Arctic Ocean, Science,356, 285–291, https://doi.org/10.1126/science.aai8204, 2017.

988   Prinsenberg, S. J. and Bennetr, E. B.: Transport between Peel Sound and Barrow Strait in the Canadian
989   Arctic, Continental Shelf Research, 427–444 pp., 1989.

990   Reeburgh, W. S., Ward, B. B., Whalen, S. C., Sandbeck, K. A., Kilpatrick, K. A., and Kerkhof, L. J.: Black
991   Sea methane geochemistry, Deep-Sea Research, Part A, 38, https://doi.org/10.1016/s0198-0149(10)80030-
992   5, 1991.

993   Repeta, D. J., Ferrón, S., Sosa, O. A., Johnson, C. G., Repeta, L. D., Acker, M., Delong, E. F., and Karl, D.
994   M.: Marine methane paradox explained by bacterial degradation of dissolved organic matter, Nat Geosci,
995   9, 884–887, https://doi.org/10.1038/ngeo2837, 2016.

996   Rogener, M. K., Bracco, A., Hunter, K. S., Saxton, M. A., and Joye, S. B.: Long-term impact of the
997   Deepwater Horizon oil well blowout on methane oxidation dynamics in the northern Gulf of Mexico,
998   Elementa, 6, https://doi.org/10.1525/elementa.332, 2018.

999   Rojo, F.: Degradation of alkanes by bacteria: Minireview, https://doi.org/10.1111/j.1462-
1000 2920.2009.01948.x, 2009.

1001 Saidi-Mehrabad, A., He, Z., Tamas, I., Sharp, C. E., Brady, A. L., Rochman, F. F., Bodrossy, L., Abell, G.
1002 C. J., Penner, T., Dong, X., Sensen, C. W., and Dunfield, P. F.: Methanotrophic bacteria in oilsands tailings
1003 ponds of northern Alberta, ISME Journal, 7, 908–921, https://doi.org/10.1038/ismej.2012.163, 2013.

1004 Sasakawa, M., Tsunogai, U., Kameyama, S., Nakagawa, F., Nojiri, Y., and Tsuda, A.: Carbon isotopic
1005 characterization for the origin of excess methane in subsurface seawater, J Geophys Res Oceans, 113,
1006 https://doi.org/10.1029/2007JC004217, 2008.

1007 Saunois, M., R. Stavert, A., Poulter, B., Bousquet, P., G. Canadell, J., B. Jackson, R., A. Raymond, P., J.
1008 Dlugokencky, E., Houweling, S., K. Patra, P., Ciais, P., K. Arora, V., Bastviken, D., Bergamaschi, P., R.
1009 Blake, D., Brailsford, G., Bruhwiler, L., M. Carlson, K., Carrol, M., Castaldi, S., Chandra, N., Crevoisier,
1010 C., M. Crill, P., Covey, K., L. Curry, C., Etiope, G., Frankenberg, C., Gedney, N., I. Hegglin, M., Höglund-
1011 Isaksson, L., Hugelius, G., Ishizawa, M., Ito, A., Janssens-Maenhout, G., M. Jensen, K., Joos, F., Kleinen,
1012 T., B. Krummel, P., L. Langenfelds, R., G. Laruelle, G., Liu, L., MacHida, T., Maksyutov, S., C. McDonald,
1013 K., McNorton, J., A. Miller, P., R. Melton, J., Morino, I., Müller, J., Murguia-Flores, F., Naik, V., Niwa,
1014 Y., Noce, S., O'Doherty, S., J. Parker, R., Peng, C., Peng, S., P. Peters, G., Prigent, C., Prinn, R., Ramonet,

1015 M., Regnier, P., J. Riley, W., A. Rosentreter, J., Segers, A., J. Simpson, I., Shi, H., J. Smith, S., Paul Steele,
1016 L., F. Thornton, B., Tian, H., Tohjima, Y., N. Tubiello, F., Tsuruta, A., Viovy, N., Voulgarakis, A., S.
1017 Weber, T., van Weele, M., R. Van Der Werf, G., F. Weiss, R., Worthy, D., Wunch, D., Yin, Y., Yoshida,
1018 Y., Zhang, W., Zhang, Z., Zhao, Y., Zheng, B., Zhu, Q., Zhu, Q., and Zhuang, Q.: The global methane
1019 budget 2000-2017, Earth Syst Sci Data, 12, 1561–1623, https://doi.org/10.5194/essd-12-1561-2020, 2020.

1020 Silyakova, A., and others. 2020. Physical controls of dynamics of methane venting from a shallow seep
1021 area west of Svalbard. Cont. Shelf Res. 194: 104030.

1022 Song, J., Choi, A., Im, M., Joung, Y., Yoshizawa, S., Cho, J. C., and Kogure, K.: Aurantivirga profunda
1023 gen. nov sp. nov isolated from deep-seawater, a novel member of the family flavobacteriaceae, Int J Syst
1024 Evol Microbiol, 65, 4850–4856, https://doi.org/10.1099/ijsem.0.000662, 2015.

1025 Sosa, O. A., Burrell, T. J., Wilson, S. T., Foreman, R. K., Karl, D. M., and Repeta, D. J.: Phosphonate
1026 cycling supports methane and ethylene supersaturation in the phosphate-depleted western North Atlantic
1027 Ocean, Limnol Oceanogr, 65, 2443–2459, https://doi.org/10.1002/lno.11463, 2020.

1028 Steinle, L., Graves, C., Treude,T., Ferre, B., Biastoch, A., Bussmann, I., Berndt, C., Krastel, S., James, R.
1029 H., Behrens, E., Böning, C.W., Greinert, J., Sapart, C-J., Scheinert, M., Sommer, S., Lehmann, Moritz F.,
1030 Niemann, H., (2015): Methane concentration, oxidation rates and abundance of bacteria during Maria S.
1031 Merian   cruise   MSM21/4   at   Svalbard   seeps   in   summer   2012.   PANGAEA,
1032 https://doi.org/10.1594/PANGAEA.844010, In supplement to: Steinle, L et al. (2015): Water column
1033 methanotrophy controlled by a rapid oceanographic switch. Nature Geoscience, 8(5), 378–382,
1034 https://doi.org/10.1038/ngeo2420

1035 Stigebrandt, A. , 1984.: [15200485 - Journal of Physical Oceanography] The North Pacific_ A Global-Scale
1036 Estuary, n.d.

1037 Sultan, N., Plaza-Faverola, A., Vadakkepuliyambatta, S., Buenz, S., and Knies, J.: Impact of tides and sea-
1038 level on deep-sea Arctic methane emissions, Nat Commun, 11, https://doi.org/10.1038/s41467-020-18899-
1039 3, 2020.

1040 Tomczak, M. A multi-parameter extension of temperature/salinity diagram techniques for the analysis of
1041 non-isopycnal mixing. *Progress in Oceanography, 10*, 147-171, 1981.

1042 Torres-Valdés, S., Tsubouchi, T., Bacon, S., Naveira-Garabato, A. C., Sanders, R., McLaughlin, F. A.,
1043 Petrie, B., Kattner, G., Azetsu-Scott, K., and Whitledge, T. E.: Export of nutrients from the Arctic Ocean,
1044 J Geophys Res Oceans, 118, 1625–1644, https://doi.org/10.1002/jgrc.20063, 2013.

1045 Uhlig, C. and Loose, B.: Using stable isotopes and gas concentrations for independent constraints on
1046 microbial methane oxidation at Arctic Ocean temperatures, Limnol. Oceanogr.: Methods, 15, 737–751,
1047 https://doi.org/10.1594/PANGAEA.874893, 2017.

1048 Uhlig, C., Kirkpatrick, J. B., D'Hondt, S., and Loose, B.: Methane-oxidizing seawater microbial
1049 communities from an Arctic shelf, Biogeosciences, 15, 3311–3329, https://doi.org/10.5194/bg-15-3311-
1050 2018, 2018.

1051 Valentine, D. L.: Biogeochemistry and microbial ecology of methane oxidation in anoxic environments: a
1052 review, Antonie van Leeuwenhoek, 271–282 pp., 2002.

1053 Wang, Y., Yu, M., Austin, B., and Zhang, X. H.: Oleispira lenta sp. nov., a novel marine bacterium isolated
1054 from Yellow sea coastal seawater in Qingdao, China, Antonie van Leeuwenhoek, International Journal of
1055 General and Molecular Microbiology, 101, 787–794, https://doi.org/10.1007/s10482-011-9693-8, 2012.

1056 Whiticar, M. J.: Carbon and hydrogen isotope systematics of bacterial formation and oxidation of methane,
1057 Chemical Geology, 291–314 pp., 1999.

1058